Monthly Notices of the ROYAL ASTRONOMICAL SOCIETY

MNRAS **544,** 988–1011 (2025) https://doi.org/10.1093/mnras/staf1739
Advance Access publication 2025 October 10

Unveiling dynamics and variability in open clusters: insights from a comprehensive analysis of six galactic clusters

Kuldeep Belwal,[1★] D. Bisht ,[1★] Ing-Guey Jiang ,[2★] R. K. S. Yadav,[3] Ashish Raj,[1,4] Geeta Rangwal,[3] Arvind K. Dattatrey ,[3,5] Mohit Singh Bisht[1] and Alok Durgapal[6]

[1]*Indian Centre for Space Physics, 466 Barakhola, Singabari Road, Netai Nagar, Kolkata 700099, India*
[2]*Department of Physics and Institute of Astronomy, National Tsing-Hua University, Hsin-Chu 30013, Taiwan*
[3]*Aryabhatta Research Institute of Observational Sciences, Manora Peak, Nainital 263129, India*
[4]*Uttar Pradesh State Institute of Forensic Science (UPSIFS), Aurawan, P.O. Banthra, Lucknow 226401, U.P, India*
[5]*Indian Institute of Astrophysics, Bangalore 560034, India*
[6]*Center of Advanced Study, Department of Physics, D. S. B. Campus, Kumaun University, Nainital 263002, India*

Accepted 2025 October 2. Received 2025 September 27; in original form 2025 June 26

ABSTRACT

We present a kinematic and dynamical analysis of six Galactic open clusters – NGC 2204, NGC 2660, NGC 2262, Czernik 32, Pismis 18, and NGC 2437, using *Gaia* DR3. We used Bayesian and Gaussian Mixture Model (GMM) methods to identify cluster members, but chose GMM because it is more appropriate for low-mass stars. Estimated distances range from 1.76 to 4.20 kpc and ages from 0.199 to 1.95 Gyr, confirming their intermediate-age nature. King model fits indicate compact morphologies, with core radii of 1–10 arcmin and cluster radii of 5–24 arcmin. We identify 13 blue straggler stars and 3 yellow straggler stars members, whose central concentrations suggest origins via mass transfer or stellar collisions. The mass function slopes (0.96–1.19) are flatter than the Salpeter value, which indicates that these clusters have undergone dynamical mass segregation. Orbit integration within a Galactic potential indicates nearly circular orbits (eccentricities 0.02–0.10), vertical excursions within $\pm$132 pc, and guiding radii near the solar circle, suggesting disc confinement. These clusters likely formed in the thin disc and are shaped by Galactic tidal perturbations, facilitating the rapid loss of low-mass members. Additionally, 12 variable stars were found across 4 clusters using *Transiting Exoplanet Survey Satellite* (*TESS*) light curves, including γ Doradus and SPB pulsators, eclipsing binaries, and a yellow straggler candidate. Periods were derived via Lomb–Scargle analysis. Two eclipsing binaries (TIC 94229743 and TIC 318170024) were modelled using PHOEBE, yielding mass ratios of 1.37 and 2.16, respectively. Our findings demonstrate that integrating orbital dynamics and variable star studies presents valuable insights into the evolutionary pathways of open clusters.

Key words: binaries: eclipsing – Hertzsprung–Russell and colour–magnitude diagrams – stars: kinematics and dynamics – stars: variables: general – open clusters and associations: general.

1 INTRODUCTION

Open clusters (OCs) are fundamental for understanding stellar evolution and formation, as they are primarily located in the Galactic disc and span a wide range of ages, covering the full lifetime of the Galactic disc (B. A. Twarog, K. M. Ashman & B. J. Anthony-Twarog 1997; K. Freeman & J. Bland-Hawthorn 2002). Older clusters trace the thick disc, while younger ones are typically found in the spiral arms of the thin disc, where perturbations are more frequent. The motion and spatial distribution of these clusters within the Galaxy help in understanding its gravitational potential and the perturbations that shape its structure and dynamics (C. Soubiran et al. 2018). Most Galactic OCs evaporate within approximately 100 Myr (R. Wielen 1971). However, clusters older than 1 Gyr are thought to have survived due to their orbital properties, which keep them away from the disruptive forces of the Galactic plane (E. Friel 1995). The dynamical evolution of stars in OCs is driven by both internal stellar processes and external influences, such as tidal forces from the Galactic disc and encounters with molecular clouds. Key dynamical processes contributing to the disruption of OCs include internal interactions among members, stellar evolution, encounters with molecular clouds, and gravitational disturbances from the Galactic potential (M. Gieles et al. 2006). OCs that survive are typically more massive, have higher central concentration, and follow orbits around the Galactic centre that minimize exposure to disruptive forces (E. Friel 1995; B. Gustafsson et al. 2016). Intermediate- and old-age OCs are especially valuable for testing theoretical stellar evolution models. Most stars in the Galaxy are believed to form clusters (S. F. Portegies Zwart, S. L. McMillan & M. Gieles 2010), making OCs natural laboratories for studying stellar development. However, since cluster stars are often contaminated by foreground and background stars, it is essential to accurately distinguish cluster members from field stars to derive reliable cluster parameters. Recent

★ E-mail: kuldeepbelwal1997@gmail.com (KB); devendrabisht297@gmail.com (DB); jiang@phys.nthu.edu.tw (IJ)

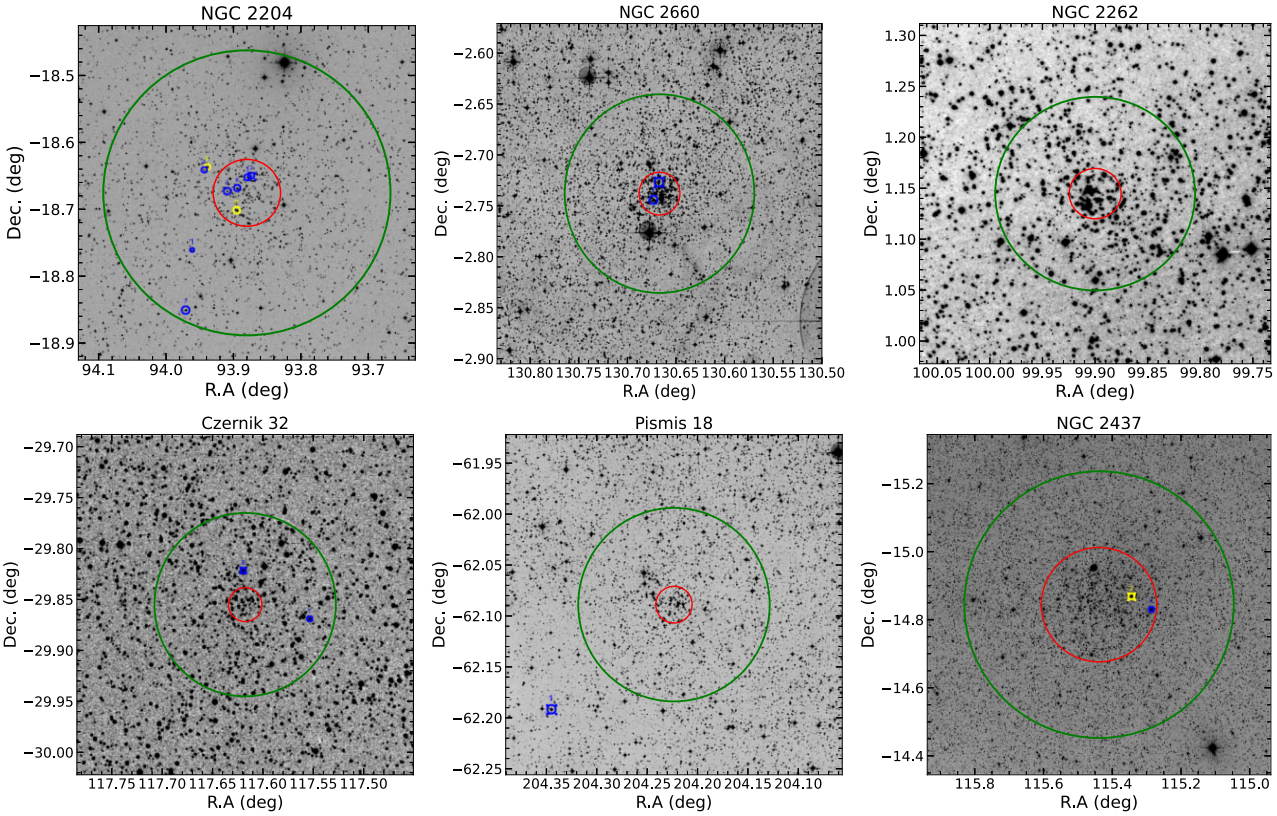

Figure 1. Identification chart of six OCs taken from the STScI Digitized Sky Survey, oriented in the north-east direction (north is up and east is left). The inner red circle represents the core radius, while the outer green ring denotes the cluster radius. The blue and yellow open circles represent the BSS and YSS, respectively.

studies have focused on membership analysis in OCs, investigating various properties (D. Bisht et al. 2019; A. Castro-Ginard et al. 2019; T. Cantat-Gaudin et al. 2020; G. Rangwal et al. 2023).

OCs host various populations of variable stars, including rotating variables, pulsating stars, eclipsing binaries, and non-periodic variables spanning a wide range of stellar masses. The detection of variable stars delivers important constraints for stellar pulsation and evolutionary models. Pulsating variables exhibit magnitude variations ranging from a few millimagnitudes (mag) to hundreds of mag, with periods from hours to days, offering valuable insights into stellar interiors and evolution as their variability arises from radial and non-radial pulsation (A. Gautschy & H. Saio 1993; Y. B. Kang et al. 2007). Intermediate-age clusters are excellent tools for analysing short-period variables. The period–luminosity relations of pulsating stars, such as Cepheids and RR Lyrae, are highly effective tools for distance measurement and studying the structure of the Galaxy (G. Iorio & V. Belokurov 2019; D. M. Skowron et al. 2019). Eclipsing binaries are valuable for testing theoretical stellar models (G. Torres, J. Andersen & A. Giménez 2010). The evolutionary link between Algol-type and W UMa-type binaries offers insights into angular momentum loss, tidal locking, and mass transfer processes in binary systems (D. Jiang, Z. Han & L. Li 2014; X. Chen et al. 2020).

This study used the six OC samples NGC 2204, NGC 2660, NGC 2262, Czernik 32, Pismis 18, and NGC 2437. These clusters are located very close to the Galactic plane. Their diverse ages, distances, and metallicities help us to trace the Galactic disc's chemical enrichment, radial abundance gradients, and star formation history, delivering fundamental insights into stellar and Galactic dynamics. The cluster identification chart is taken from the Digitized Sky Survey (DSS)[1] and shown in Fig. 1. The available information about these clusters in the literature is discussed here:

NGC 2204

NGC 2204 (C0613–186) is located in the constellation of Canis Major ($\alpha_{2000} = 06^{h}15^{m}33^{s}$, $\delta_{2000} = -18^{\circ}39'54''$) and corresponding Galactic coordinates ($l = 226.^{\circ}0208$, $b = -16^{\circ}.1143$). The calculated parameters in the literature for the age, reddening, and distance range vary from 1.85 to 2.08 Gyr, 0.1 to 0.2 mag, and 3.90 to 4.20 kpc, respectively. M. Angelo et al. (2023) estimated the cluster's core radius and distance modulus to be 4.81 ± 0.82 arcmin and 13.03 ± 0.15 mag, respectively, and B. J. Anthony-Twarog et al. (2024) reported the radial velocity 90.9 ± 1.94 km s^{-1}. In this cluster, V. V. Jadhav et al. (2021) found six, and M. Rain, J. Ahumada & G. Carraro (2021) found seven blue straggler stars (BSSs) and two yellow straggler stars (YSSs).

NGC 2660

NGC 2660 (C0840–469) is situated in the constellation of Vela ($\alpha_{2000} = 08^{h}42^{m}38^{s}$, $\delta_{2000} = -47^{\circ}12'00''$) and corresponding Galactic coordinates ($l = 265^{\circ}.931$, $b = -03^{\circ}.015$). The estimated parameters in literature age, reddening, and distance range vary from 0.93 to 1.64 Gyr, 0.4 to 0.5 mag, and 2.6 to 2.8 kpc, respectively (S. Sandrelli et al. 1999; E. J. Jeffery et al. 2016; T. Cantat-Gaudin et al. 2020; W. S. Dias et al. 2021). M. Angelo et al. (2023) estimated the

[1] https://archive.stsci.edu/dss/

cluster's core radius, half-mass radius, and distance modulus to be 0.86 ± 0.21 arcmin and 2.04 ± 0.35 parsec and 11.96 ± 0.25 mag, respectively. In this cluster V. V. Jadhav et al. (2021) found one and M. Rain et al. (2021) found two BSSs. In the study by A. Bragaglia et al. (2024), the radial velocity of this cluster is reported to be 22.47 $\pm$ 0.27 km s^{-1}.

NGC 2262

NGC 2262 (C0635+012) is located in the constellation of Puppis ($\alpha_{2000} = 06^{h}39^{m}38^{s}$, $\delta_{2000} = +01°08'36''$) and corresponding Galactic coordinates ($l = 245.°8931$, $b = -1°.7398$). The estimated parameters age, reddening, distance modulus, and distance range vary from 0.645 to 1.17 Gyr, 0.55 to 0.63 mag, 12.54 to 14.50 mag, and 2.51 to 3.6 kpc, respectively, given by G. Carraro et al. (2005), S. Hoq & D. Clemens (2015), T. Cantat-Gaudin et al. (2020), and W. S. Dias et al. (2021). The radial velocity of this cluster has been reported as 53.64 ± 2.05 km s^{-1} in the study conducted by J. Zhong et al. (2020).

Czernik 32

Czernik 32 (C0748–297) is located in the constellation of Puppis ($\alpha_{2000} = 07^{h}50^{m}30^{s}$, $\delta_{2000} = -29°51'00''$) and corresponding Galactic coordinates ($l = 245.°893$, $b = -1°.7398$). The estimated parameters age, reddening, distance modulus, distance, and Galactic distance range vary from 1.08 to 1.35 Gyr, 0.66 to 0.85 mag, 12.5 to 15.7 mag, 3.16 to 4.14 kpc, and 9.75 to 10.80 kpc, respectively, given by E. Bica & C. Bonatto (2005), G. Carraro et al. (2005), M. Angelo, J. Santos Jr & W. Corradi (2020), and T. Cantat-Gaudin et al. (2020). In this cluster V. V. Jadhav et al. (2021) found two BSSs.

Pismis 18

Pismis 18 (C1333–619) is located in the constellation of Centaurus ($\alpha_{2000} = 13^{h}36^{m}55^{s}$, $\delta_{2000} = -62°05'36''$), with corresponding Galactic coordinates ($l = 308°.226$, $b = 0°.3134$). As an intermediate-age open cluster, its estimated distance, reddening ($E(B-V)$), and age fall within the ranges of 1.79–2.47 kpc, 0.50–0.61 mag, and 0.70–1.2 Gyr, respectively, given by A. E. Piatti et al. (1998), D. Hatzidimitriou et al. (2019), T. Cantat-Gaudin et al. (2020), and W. S. Dias et al. (2021). A. L. Tadross (2008) estimated the cluster's radius to be 5.6 arcmin, while D. Hatzidimitriou et al. (2019) reported a radius of approximately 5.0 arcmin and a metallicity [Fe/H] of 0.23 ± 0.05 dex. Using 26 high-confidence members, D. Hatzidimitriou et al. (2019) estimated the radial velocity to be -27.5 ± 2.5 km s^{-1}.

NGC 2437

NGC 2437 (C0739–147) is located in the constellation of Puppis ($\alpha_{2000} = 07^{h}41^{m}46^{s}$, $\delta_{2000} = -14°48'36''$), and corresponding Galactic coordinates ($l = 231°.889$, $b = 4°.0493$). A young rich cluster with an estimated age, reddening, and distance ranging from 0.199 to 0.302 Gyr, 0.12 to 0.20 mag, and 1.5 to 1.7 kpc, respectively, given by S. Sharma et al. (2006), T. Davidge (2013), T. Cantat-Gaudin et al. (2020), and V. V. Jadhav et al. (2021). N. Sánchez, E. J. Alfaro & F. López-Martínez (2020) estimated the cluster's radius to be around 25 arcmin. In this cluster, M. Rain et al. (2021) found one BSS and one YSS. The cluster may also be physically associated with the nearby planetary nebula NGC 2438 (C. Bonatto, E. Bica & J. F. Santos Jr 2008).

The selection of this sample was guided by several considerations. First, these are relatively rich, intermediate-age to old OCs that had been studied in the pre-*Gaia* era. At that time, measurements of proper motion and parallax were significantly less precise. Revisiting these clusters with *Gaia* DR3 allows us to derive far more accurate astrometric and photometric parameters. This leads to an improved characterization of their kinematical and dynamical properties. Second, the clusters lie close to the Galactic plane, where their fields are strongly contaminated by foreground and background stars. *Gaia*'s high-precision data are essential for robust membership determination. Third, *Transiting Exoplanet Survey Satellite* (*TESS*) observations serve as an independent data set that strengthens our characterization of stellar variability. This is particularly useful for detecting eclipsing binaries and variable stars that serve as additional probes of the stellar populations. Finally, the chosen systems span a range of ages, total masses, and Galactocentric positions. This offers a representative set to explore how structural and dynamical properties evolve under different conditions within the Galactic disc. Together, these criteria ensure that the present study provides accurate and comprehensive insights into the internal dynamics and evolutionary states of Galactic open clusters.

This study presents a photometric analysis of six OCs, focusing on their spatial structure, fundamental parameters, and age to gain insight into their dynamical evolution. Membership probabilities were estimated for stars within the clusters down to G ∼20 mag. Highly probable members were employed to analyse the mass function and investigate mass segregation.

The paper is organized as follows: Section 2 describes the data used in this study. Section 3 discusses the determination of stellar membership within the clusters. Section 4 derives the structural parameters of the clusters. Section 5 presents distance estimates based on parallax measurements, while physical parameters such as age and photometric distance are derived using theoretical isochrone fitting and the location of the BSS within the cluster, as discussed in Section 6. Section 7 examines the dynamical evolution of the clusters. Section 8 discusses the identification and classification of variable stars, as well as light curve modelling. Finally, we present a comparative discussion of the six clusters in Section 9, and the main findings are summarized in Section 10.

2 DATA SOURCES AND SELECTION CRITERIA

2.1 *Gaia* DR3

Gaia DR3 (Gaia Collaboration 2023) is used for the photometric and astrometric study of all clusters and for determining their structural parameters. *Gaia* DR3 provided celestial positions and *G*-band magnitudes for a vast data set of around 1.8 billion sources, with a magnitude measurement extending up to 21 mag. Additionally, *Gaia* DR3 provides valuable parallax, proper motion, and colour information (G_{BP}–G_{RP}) for a sub-set of this data set, specifically for 1.5 billion sources. The uncertainties in parallax values are ∼0.02–0.03 milli arcsecond (mas) for sources at $G \leq 15$ mag and ∼0.07 mas for sources with $G \sim 17$ mag. The adopted search radii were chosen with reference to cluster sizes reported in the literature. Specifically, the reported radii are 9.3 arcmin for NGC 2204 (N. Kharchenko et al. 2013), 4.3 arcmin for NGC 2660 (N. Sánchez et al. 2020), 1.0 arcmin for NGC 2262 (G. Carraro et al. 2005), 4.75 arcmin for Czernik 32 (N. Sánchez et al. 2020), and for Pismis 18, values of 5.6 and 5.0 arcmin are given by A. L. Tadross (2008) and D. Hatzidimitriou et al. (2019), respectively. For NGC 2437, a radius of 25.5 arcmin is reported by N. Sánchez et al. (2020). These literature values guided our choice of extraction radii, which ranged from 10 to 30 arcmin, adopted in this study. We applied several selection criteria to collect the data, including a renormalized unit weight error (RUWE) factor of ≤1.4 (L. Lindegren et al. 2021), parallax ≥0, proper motion error ≤0.6, and *G* magnitude ≤20.2. The uncertainties in the corresponding proper motion components are ∼0.01–0.02 (for $G \leq 15$ mag), ∼0.05 (for *G*

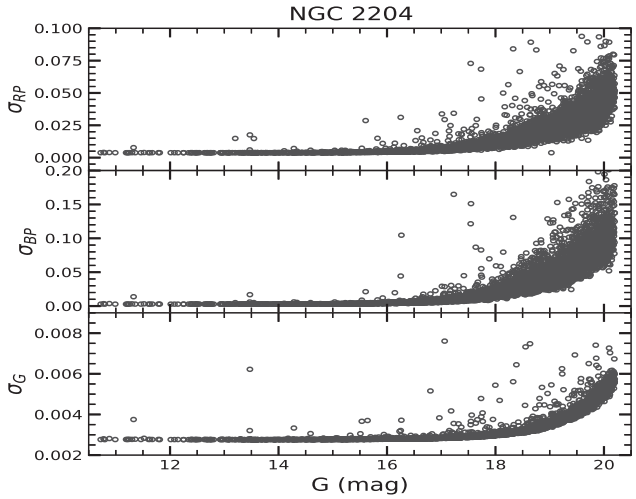

Figure 2. Photometric uncertainties in the G, G_{BP}, and G_{RP} bands plotted as a function of G magnitude for stars in the open cluster NGC 2204.

$\sim$ 17 mag), $\sim$0.4 (for $G \sim 20$ mag), and $\sim$1.4 mas yr^{-1} (for $G \sim 21$ mag). For cluster Pismis 18, we observed that at the fainter end of the G magnitude range (17 to 20), the associated photometric error exceeds 0.01 mag. In contrast, the error remains below 0.01 mag within the same magnitude range in the G band for the remaining clusters. To illustrate this trend, a reference plot for NGC 2204 is presented in Fig. 2.

We cross-matched our cluster members with the *Gaia* DR3 variability catalogue. Among all stars analysed in this work, only a single source (TIC 318170024) is flagged as variable in *Gaia*, while no variability information is available for the remaining stars. We also examined the astrometric quality indicator RUWE for all selected members. In every case, the RUWE values are $\leq$1.4, confirming that the stars included in our study have reliable *Gaia* astrometry. This ensures that spurious or poor-quality solutions do not compromise our membership selection.

2.2 *TESS* data

Transiting Exoplanet Survey Satellite (*TESS*) is an almost all-sky photometric survey primarily focused on detecting transiting exoplanets (G. R. Ricker et al. 2015). *TESS* observes each 24° × 96° sector for approximately 27 d of near-continuous monitoring. It is equipped with four identical cameras, each covering a 24° × 24° field of view. One camera contains four CCDs that generate 2048 × 2048 pixel images with a pixel scale of 21 arcsec. During the primary mission (Sectors 1–26), full-frame images (FFIs) were acquired with a 30-min cadence. In the first extended mission (Sectors 27–55), the cadence was shortened to 10 min. Beginning with Cycle 5 (Sectors 56 and beyond), the duration was further reduced to 200 s. Photometric data are available for sources brighter than approximately 17th magnitude in the *TESS* bandpass, which spans 600–1000 nm and is centred on the Cousins *I* band. In the present study, we utilize *TESS* photometric data to investigate the stellar variability and properties of the open clusters NGC 2204, NGC 2262, Pismis 18, and NGC 2437. Specifically, we use the 30-min cadence FFIs from Sectors 1–26 and the 10-min cadence FFIs from Sectors 27–39, processed by the *TESS* Science Processing Operations Centre (SPOC) FFI pipeline.[2]

[2]https://heasarc.gsfc.nasa.gov/docs/tess/documentation.html

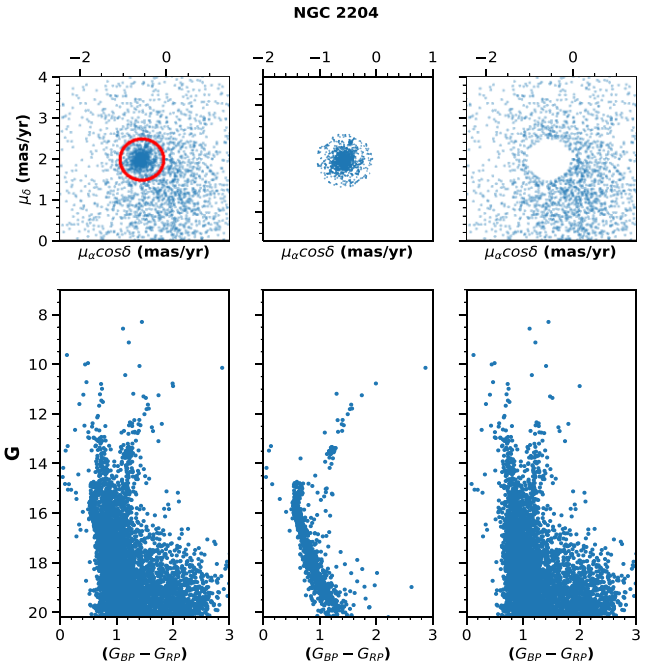

Figure 3. This figure illustrates the initial cluster member separation method based on *Gaia*'s proper motions for the cluster. The top panel displays the VPDs, while the bottom panels show the *Gaia* CMDs for the total stars, cluster members, and field stars. In the top panel, a circle with a radius of 0.5 mas yr^{-1} represents the member stars within the cluster field.

3 MEMBERSHIP PROBABILITY

3.1 Bayesian method

OCs, mostly in the Galactic disc, are usually contaminated by foreground and background stars. To derive the actual parameters of the cluster, we need to separate the cluster stars from the field stars. The stars of clusters have the same kinematical properties as well as the same heliocentric distance. Hence, proper motion and parallax of stars can be used to differentiate cluster members from field stars. We utilized parallax and proper motion data from the *Gaia* DR3 catalogue to select member stars of the clusters in this study. We used the maximum likelihood method described by L. Balaguer-Núnez, K. Tian & J. Zhao (1998) for these clusters. Previous studies (D. P. Sariya et al. 2021; D. Bisht et al. 2021a, b, 2022b; and N. Panwar et al. 2024) used this method in their analysis. This method relies entirely on the proper motion of stars, with *Gaia* DR3 providing precise measurements of astrometric parameters.

We discussed this method in K. Belwal et al. (2024) to calculate the membership probability of stars in the cluster region. We define a circular region around the concentrated clustering region in proper motion space; the radius of the circle is based on $r = \sqrt{r_0^2 + \sigma^2}$, where r_0 is based on visual inspection and σ is an error in proper motion. We have chosen the radii of each circle as 0.6, 0.6, 0.55, 0.45, 0.5, and 0.5 mas yr^{-1} for NGC 2204, NGC 2660, NGC 2262, Czernik 32, Pismis 18, and NGC 2437, respectively. In Fig. 3, we present the vector point diagram (VPDs) for NGC 2204.

After selecting stars within the circle of the VPDs, we applied an additional selection criterion based on the mean parallax value. We calculated the arithmetic mean of the parallaxes for the stars within the VPD circle with G magnitudes brighter than 20 mag. A star is considered a most probable cluster member if its parallax angle is within 3σ of the mean parallax value. In this way, we get the actual

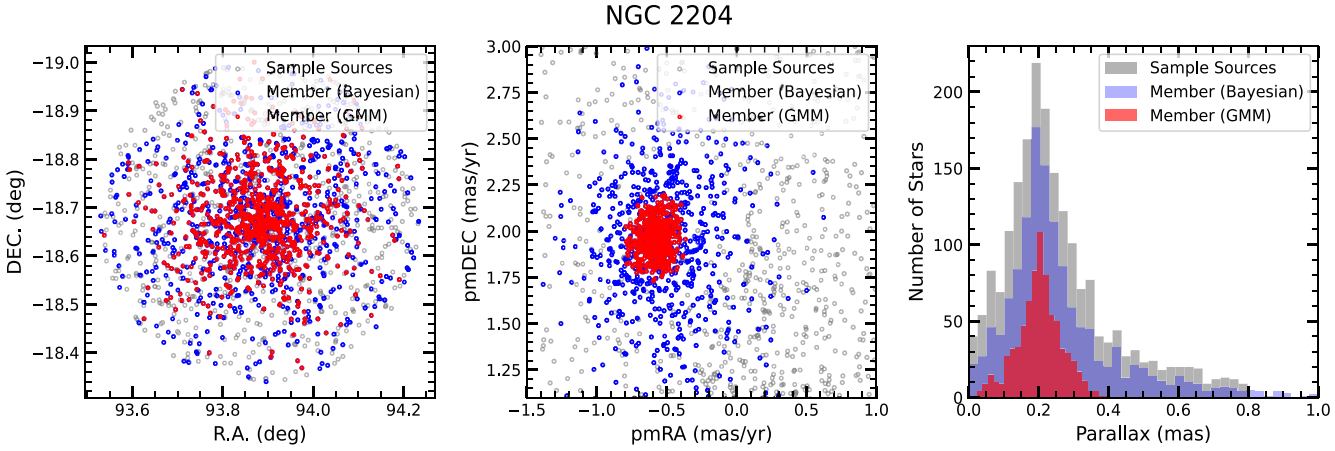

Figure 4. Membership analysis of the open cluster NGC 2204. Panel (a) shows the spatial distribution of stars in R.A. and Dec., panel (b) displays the proper motion distribution in the $\mu_\alpha \cos\delta$ versus μ_δ plane, and panel (c) presents the parallax distribution. The results from the GMM-based method and the Bayesian approach (ML-MOC) are compared, with red and blue dots indicating high probability members identified by each method, respectively, and grey points representing the full sample.

number of probable cluster members. We plotted histograms for each cluster to estimate the mean proper motion values. A Gaussian function was fitted to the histograms of proper motions ($\mu_\alpha \cos\delta$ and μ_δ), yielding the mean values and standard deviations for each cluster. The estimated mean proper motions (in mas yr^{-1}) are as follows: -0.56 ± 0.31, 1.96 ± 0.32 for NGC 2204; -2.74 ± 0.20, 5.20 ± 0.27 for NGC 2660; 0.28 ± 0.11, 0.11 ± 0.17 for NGC 2262; -2.95 ± 0.21, 2.49 ± 0.15 for Czernik 32; -5.69 ± 0.25, -2.25 ± 0.30 for Pismis 18; and -3.87 ± 0.18, 0.41 ± 0.19 for NGC 2437. Our estimated values of PMs are in good agreement with those reported by T. Cantat-Gaudin et al. (2020) and W. S. Dias et al. (2021). The corresponding dispersions in proper motions (σ_c) are 0.09, 0.06, 0.08, 0.09, 0.11, and 0.10 mas yr^{-1}, assuming distances of 4.20, 2.95, 3.29, 4.02, 2.91, and 1.76 kpc, respectively. We adopted a radial velocity dispersion of 1 km s^{-1}, following T. M. Girard et al. (1989). This choice is motivated by observational evidence that intermediate-age and old OCs typically exhibit internal velocity dispersions in the range 0.5–2 km s^{-1} (e.g. A. M. Geller et al. 2010). Using the relation $\sigma^2 = GM/R$, where G is the gravitational constant, M is the cluster mass, and R is the half-mass radius, we independently estimated the radial velocity dispersion for our clusters. We obtained values close to $\sim$1 km s^{-1}, consistent with T. M. Girard et al. (1989). Tests with alternative dispersions within this range (0.5–2 km s^{-1}) indicate that the membership probabilities remain robust, although adopting significantly larger values increases contamination from field stars.

For field stars, the proper motion centres (μ_{xf}, μ_{yf}) are (0.11, 1.04), (-3.25, 3.78), (-0.22, -0.03), (-1.50, 2.02), (-6.50, -1.62), and (-1.42, 1.18), while the corresponding dispersions (σ_{xf}, σ_{yf}) are (3.24, 4.05), (3.30, 3.91), (0.64, 0.98), (0.95, 1.06), (3.34, 1.50), and (3.46, 4.95), respectively. We have used the equation provided by (R. Yadav, D. P. Sariya & R. Sagar 2013) to calculate the membership probability. Based on a membership probability threshold of $\geq$70 per cent, we identified 1326, 1078, 560, 680, 1137, and 2470 member stars in the respective clusters. In Fig. 4, the Bayesian 70 per cent member stars are represented by blue open circles, showing their spatial distribution compared to the GMM-based 70 per cent probable members.

Regarding the membership probability threshold, we adopted a cut-off of 70 per cent to select high-confidence cluster members.

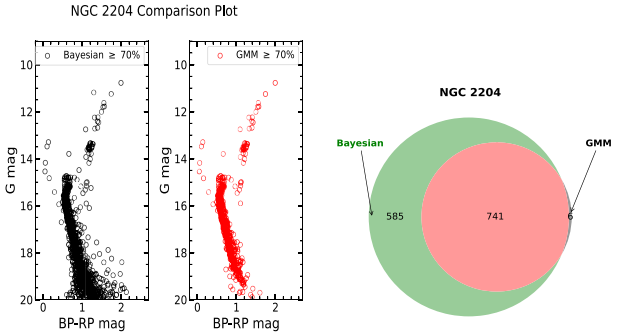

Figure 5. A comparison of the CMDs from both methods is shown on the left, displaying stars with a membership probability greater than 70 per cent. The Venn diagram for the cluster NGC 2204 is presented on the right.

This threshold is widely used in the literature (e.g. A. Castro-Ginard et al. 2019; D. Bisht et al. 2020; T. Cantat-Gaudin et al. 2020) as it provides a balance between maximizing completeness and minimizing field-star contamination. We also tested thresholds between 50 per cent and 90 per cent, finding that lower thresholds include more faint members but increase contamination, whereas higher thresholds reduce contamination but exclude some genuine faint members. Thus, 70 per cent provides an optimal compromise for our analysis.

In the Bayesian membership estimation, we found residual contamination from field stars, particularly at faint magnitudes ($G \sim$ 18–20). For example, applying a probability threshold of $P \geq 0.7$ left $\sim$15–16 per cent of stars lying outside the expected cluster sequence in the colour–magnitude diagram (CMD), indicative of field contamination. By contrast, the Gaussian Mixture Model (GMM) method reduced this fraction to $\sim$4–5 per cent, producing a much cleaner main sequence, especially at the faint end as shown in Fig. 5. To mitigate this issue, we therefore adopted the GMM approach to refine our membership determination. A detailed description of the GMM methodology is provided in the following section.

3.2 Gaussian Mixture Model

This approach does not require any prior information about cluster parameters. Instead, it relies on modeling the cluster and field stars as two distinct Gaussian distributions in proper motion and parallax space. We have adopted the method described in M. Agarwal et al. (2021), which has also been widely used in previous studies, as referenced by X. Gao (2018), J.-S. Qiu et al. (2024), and A. Sheikh, S. Deka & B. J. Medhi (2025). First, we extracted sample sources from the entire data set by applying the *k*-Nearest Neighbours (*k*NNs) algorithm and removing field star noise. Then, we normalized the proper motion and parallax data before using the GMM.

3.2.1 Source extraction

First, we downloaded data from *Gaia* DR3 for a cone-shaped region centred on each cluster, using different radii based on literature values: 30 arcmin for NGC 2437, 20 arcmin for NGC 2204, and 10 arcmin for NGC 2260, NGC 2262, Pismis 18, and Czernik 32. We then removed field star noise from the downloaded data set by applying the following criteria:

(i) Each source must have all five astrometric parameters: right ascension, declination, proper motion in right ascension and declination, and parallax, as well as photometric magnitudes in three bands: G, G_{BP}, G_{RP}.

(ii) Parallax must be positive, the proper motion error must be $\leq$1.0, and the G-band magnitude error must be $\leq$0.008.

To estimate the mean values of proper motion and parallax for the cluster members, we employed the *k*NN algorithm (T. Cover & P. Hart 1967). This algorithm is based on Euclidean distance and calculates the distance of each point to its *k*NN for classification and regression purposes. The data point with the smallest total distance, defined as the sum of distances to its *k*NNs, was used to make a preliminary estimation of the cluster parameters. We applied the *k*NN algorithm in the three-dimensional space of proper motion and parallax to determine the initial mean parameters of this space. For this, we considered stars within a 10 arcmin radius, where the cluster population dominates over field stars. The estimated mean parameters show good agreement with those reported by T. Cantat-Gaudin et al. (2020) and E. L. Hunt & S. Reffert (2023).

The sample selection range of 1.5 to 3.5 mas yr^{-1} was iteratively adjusted by sliding the window in proper motion to converge on the most likely mean value, as determined by the *k*NN algorithm. Similarly, the parallax range was selected using an initial window whose width depended on the estimated cluster parallax mean value from *k*NN – wider for nearby clusters and narrower for distant ones. The final parallax range spanned a width between 0.4 and 1.5 mas. As a result, we obtained a refined sample of sources for the subsequent steps.

3.2.2 Normalization and GMM implementation

We applied the GMM (G. McLachlan 2000), an unsupervised clustering algorithm, to separate the cluster stars from the sample sources. First, the selected data for parallax and proper motion parameters were normalized. Given N sample sources, each with m parameters $x = x^1, x^2, x^3, \ldots, x^m$, the normalization for the jth dimension was defined as X_i^j (M. Agarwal et al. 2021)

$$X_i^j = \frac{x_i^j - \mu^j}{\sigma^j} \quad (i = 1, 2, ..., N; j = 1, 2, ...m) \tag{1}$$

where x_i^j initial parameter and μ^j is the median of x^j and σ^j is its standard deviation.

A GMM is a statistical technique that models data drawn from a combination of several Gaussian distributions, each with its own set of unknown parameters. Unlike K-Means clustering (J. MacQueen & others 1967; S. Lloyd 1982), which focuses only on the mean (μ) to define clusters, GMM also accounts for the covariance (Σ), capturing the shape and orientation of each cluster in the data. The model is fitted by maximizing the likelihood estimates of the distribution parameters using the expectation–maximization (EM) algorithm (A. P. Dempster, N. M. Laird & D. B. Rubin 1977). Given N data points $x = x_1, x_2, x_3, \ldots, x_N$ in a parameter space of M dimensions, the K-component GMM is defined as

$$P(x) = \sum_{i=1}^{K} w_i G(x \mid \mu_i, \Sigma_i), \quad \text{such that} \quad \sum_{i=1}^{K} w_i = 1, \tag{2}$$

Here, $P(x)$ represents the probability distribution of the data points x, w_i denotes the weight of the ith Gaussian component in the mixture, and $G(x \mid \mu_i, \Sigma_i)$ is the Gaussian distribution associated with the ith component.

$$G(x \mid \mu_i, \Sigma_i) = \frac{\exp\left[-\frac{1}{2}(x - \mu_i)^T \Sigma_i^{-1}(x - \mu_i)\right]}{(2\pi)^{M/2}\sqrt{|\Sigma_i|}} \tag{3}$$

Here, μ_i and Σ_i designate the mean vector and the full covariance matrix of the ith Gaussian component, respectively. The GMM delivers a soft membership probability for each data point, reflecting the likelihood of its connection with each cluster.

To reliably estimate the membership probability of cluster members within the sample sources, we adhered to the following initial conditions: (1) using high-precision data sets, (2) ensuring a high proportion of cluster members relative to field sources, i.e. a high cluster-to-field source ratio, and (3) ensuring distinct peak locations in the distributions of cluster and field stars (E. Graeve 1979). If these conditions are not met, the estimated membership probabilities may lose reliability and significance. We utilized the exceptional quality of *Gaia* DR3 data to fulfil the first condition in our analysis. We ensured a high proportion of cluster stars for the sample selection and then applied the GMM to the selected sources. As shown in the histogram plot in Fig. 4 and the other figures in the Appendix A, the parameters exhibit distinct distributions for cluster and field stars, confirming that all three conditions were fully satisfied. We employed a two-component GMM to represent the cluster and field populations in the normalized three-dimensional parameter space ($\mu_\alpha^*, \mu_\delta, \bar{\omega}$). This method assumes that the proper motions and parallaxes of the sample sources follow a two-component Gaussian distribution. Positional data were excluded from the parameter space to avoid confining cluster members within a fixed ellipsoidal boundary, allowing us to study the cluster's morphology and identify potential escapers (M. Agarwal et al. 2021). We considered only stars with a membership probability $\geq$70 per cent for further analysis in this study. We used 70 per cent of the member stars to estimate the mean values of right ascension, declination, parallax, and proper motion for the cluster stars listed in Table 1, showing good agreement with the values reported by T. Cantat-Gaudin et al. (2020) and E. L. Hunt & S. Reffert (2023).

To estimate cluster memberships, we applied both the Bayesian and the GMM method. A comparison of the two methods is shown in Fig. 5, for NGC 2204, with results for the other clusters provided in Appendix B. The left panel of Fig. 5 presents the CMD distributions of members identified by each method. In contrast, the right panel shows a Venn diagram illustrating their overlap, following the

Table 1. Mean astrometric and kinematic parameters of selected open clusters derived using stars with a membership probability greater than 70 per cent as identified by the GMM method. The parameters include the cluster centre coordinates (RA and Dec.), proper motions in right ascension (pmRA) and declination (pmDec.), parallax, and radial velocities (RVs). The uncertainties represent the standard error of the mean.

Cluster	RA deg.	Dec. deg.	pmRA mas yr^{-1}	pmDec. mas yr^{-1}	Parallax mas	RVs km s^{-1}
NGC 2204	93.880 ± 0.050	-18.675 ± 0.067	-0.58 ± 0.07	1.96 ± 0.12	0.202 ± 0.07	92.32 ± 2.29
NGC 2660	130.667 ± 0.06	-47.196 ± 0.04	-2.74 ± 0.20	5.20 ± 0.27	0.33 ± 0.10	22.66 ± 5.43
NGC 2262	99.899 ± 0.039	1.145 ± 0.035	0.30 ± 0.11	0.11 ± 0.10	0.26 ± 0.11	63.94 ± 3.76
Czernik 32	117.617 ± 0.059	-29.855 ± 0.070	-2.96 ± 0.18	2.48 ± 0.15	0.22 ± 0.12	72.29 ± 4.69
Pismis 18	204.223 ± 0.134	-62.089 ± 0.064	-5.69 ± 0.22	-2.35 ± 0.21	0.35 ± 0.10	-24.70 ± 8.50
NGC 2437	115.438 ± 0.174	-14.844 ± 0.175	-3.87 ± 0.18	0.41 ± 0.19	0.60 ± 0.07	45.15 ± 15.75

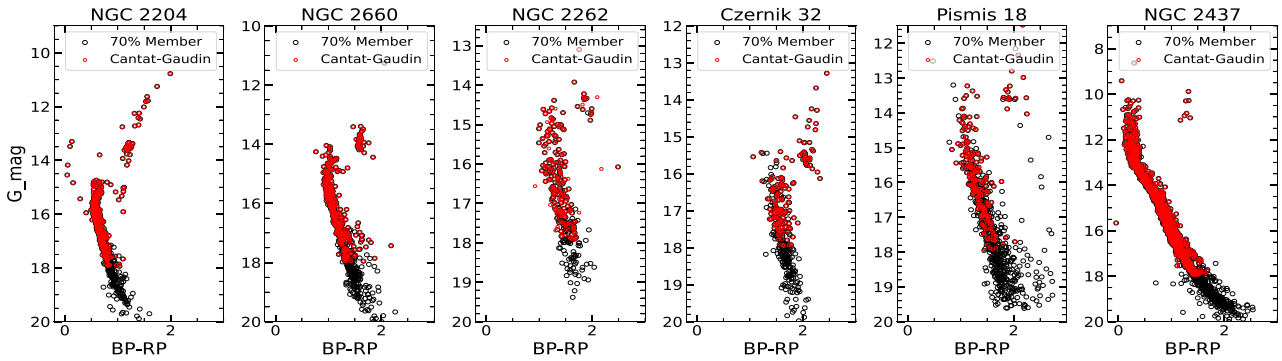

Figure 6. Colour–magnitude diagrams (CMDs) for the clusters NGC 2204, NGC 2060, NGC 2262, Czernik 32, Pismis 18, and NGC 2437. Black points represent the stars from our analysis, while red points indicate the matched members from the T. Cantat-Gaudin et al. (2020) catalogue. The good agreement between data sets confirms our membership results.

approach of J.-S. Qiu et al. (2024). For NGC 2204, 741 of 747 stars (99.1 per cent) selected by the GMM are also identified by the Bayesian method, whereas only 585 of 1326 stars (44.1 per cent) from the Bayesian sample are recovered by the GMM. This pattern is consistent across all clusters, with GMM overlaps ranging from 85 to 99 per cent compared to 36 to 79 per cent for the Bayesian method. The Bayesian approach includes a larger number of stars, particularly at faint magnitudes ($G \geq 18$ mag) and in the cluster periphery, owing to its weaker selection criteria, which often admit field contamination. In contrast, the GMM employs stricter thresholds that effectively reduce field star contamination. Therefore, we adopt the GMM-derived memberships for the subsequent mass function and structural analyses, as they provide a more reliable separation between cluster members and field stars. Our analysis yields similar outcomes, confirming the conclusion of J.-S. Qiu et al. (2024) that the Bayesian approach admits more field stars, especially at fainter magnitudes.

We compared GMM-selected member stars with those identified by T. Cantat-Gaudin et al. (2020), as shown in Fig. 6, where the matched stars are highlighted using red open circles. The comparison shows a strong agreement between the estimated parameters, thereby further validating our member selection method. Through cross-matching, we identified 500, 370, 203, 155, 230, and 1365 common member stars for the clusters NGC 2204, NGC 2660, NGC 2262, Czernik 32, Pismis 18, and NGC 2437, respectively.

4 STRUCTURAL ANALYSIS OF CLUSTERS

OCs are loosely bound systems with thinly dispersed stars, but the stellar density is observed to be highest at the centre. Determine the cluster centre using the right ascension and declination of the 70 per cent most probable members and estimate the mean values through Gaussian curve fitting. It provides the mean value and standard deviation used as a cluster centre, as shown in Table 2. We collected data for each cluster at various scales to determine the true extent of the cluster radius and derive the radial density profile (RDP). We divided the entire cluster area into concentric rings of 1 arcmin width, using the cluster centre as the reference point. The stellar density in each ring is estimated by dividing the number of stars in the ring by the area of that specific ring $\rho_i = N_i/A_i$. Where N_i is number of stars and A_i area of the ith zone. The structural parameters of the cluster are derived by fitting the I. King (1962) profile to the RDP, as shown in Fig. 7. The King's profile is given by

$$f(r) = f_0 \left[\frac{1}{\sqrt{1+(r/r_c)^2}} - \frac{1}{\sqrt{1+(r_t/r_c)^2}} \right]^2 + f_b. \quad (4)$$

Where f_b represents the background density, r_c denotes the core radius, f_0 is the central density, and r_t corresponds to the tidal radius. The cluster radius (r_{cl}) is defined as the distance from the cluster centre at which the stellar density equals the background density, ranging from 5.4 to 23.5 arcmin. The core radius is the distance from the cluster centre where the density drops to half of the central density, varying from 1.0 to 10.1 arcmin. Table 2 provides all the calculated structural parameter values. Our estimated values of the core radius and cluster radius are consistent with the reported uncertainties in the literature (A. L. Tadross 2008; D. Hatzidimitriou et al. 2019; N. Sánchez et al. 2020; M. Angelo et al. 2023).

We have calculated the density contrast parameter, δ_c, for each cluster using the formula described in C. Bonatto & E. Bica (2007). This parameter provides insight into the compactness and sparseness of the clusters. The calculated values range from $21 \leq \delta_c \leq 70$. All the clusters analysed in this study are compact based on these values.

Table 2. Structural parameters of the open clusters under study, derived from stellar radial density profiles. Listed parameters include central stellar density (f_0), background density (f_b), core radius (r_c), cluster radius (r_{cl}), and tidal radius (r_t), with associated uncertainties. These values provide insights into the stellar concentration and spatial extent of each cluster.

Parameters	NGC 2204	NGC 2660	NGC 2262	Czernik 32	Pismis 18	NGC 2437
Central density(f_0) number/arcmin^2	8.46 ± 0.48	41.90 ± 3.04	28.65 ± 5.16	28.32 ± 1.46	22.98 ± 1.59	7.30 ± 1.44
Background density(f_b) number/arcmin^2	0.20 ± 0.12	1.20 ± 0.30	0.41 ± 0.30	0.45 ± 0.28	0.70 ± 0.24	0.21 ± 0.10
Core radius(r_c) arcmin	3.00 ± 0.10	1.20 ± 0.20	1.47 ± 0.20	1.00 ± 0.20	1.00 ± 0.10	10.1 ± 0.20
Core radius(r_c) parsec	3.70 ± 0.15	1.02 ± 0.17	1.41 ± 0.20	1.17 ± 0.24	0.85 ± 0.1	5.17 ± 0.20
Cluster radius(r_{cl}) arcmin	12.80 ± 1.20	5.80 ± 0.50	5.60 ± 0.50	5.40 ± 0.70	5.60 ± 0.60	23.5 ± 2.10
Cluster radius(r_{cl}) parsec	15.64 ± 1.45	4.97 ± 0.43	5.35 ± 0.48	6.31 ± 0.82	4.74 ± 0.51	12.03 ± 1.50
Tidal radius(r_t) arcmin	17.28 ± 2.20	12.21 ± 2.05	8.80 ± 1.80	8.39 ± 1.11	11.78 ± 1.71	34.73 ± 3.50
Tidal radius(r_t) parsec	20.63 ± 2.50	10.48 ± 1.76	8.28 ± 1.95	9.81 ± 1.30	9.98 ± 1.45	17.78 ± 1.80

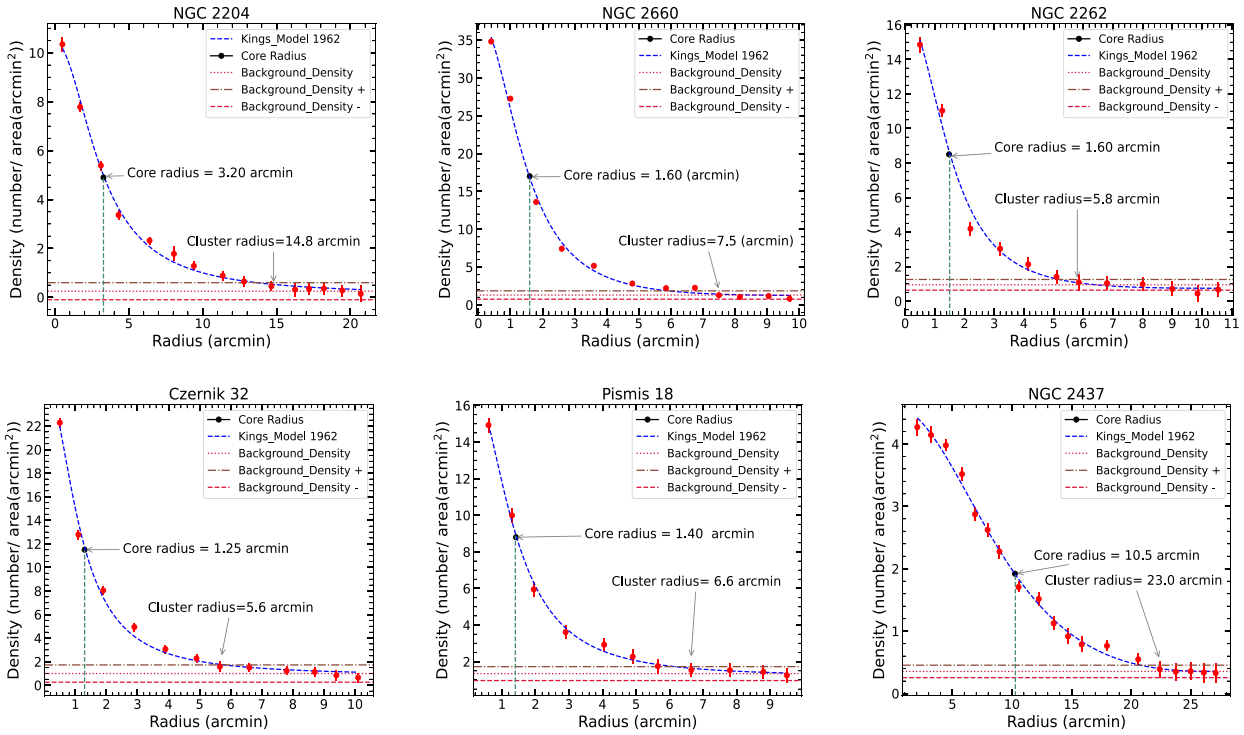

Figure 7. Radial density profiles of the studied clusters fitted with the empirical King (1962) model, shown as the solid blue curve. The core radius (r_c) and cluster radius (r_{cl}) are estimated from the fit. Horizontal dashed lines represent the background stellar density level, with shaded regions indicating the associated uncertainties. Each panel corresponds to one cluster as labelled.

5 PARALLAX-BASED DISTANCE ESTIMATION

Parallax is a key parameter of an open cluster, and the relationship between distance and parallax is straightforward: the distance can be calculated by inverting the parallax under ideal conditions without accounting for measurement uncertainties. Measurement errors are mandatory, and determining the distance from parallax values becomes a complex task that requires careful consideration of uncertainties (C. Bailer-Jones et al. 2018). In this analysis, we consider the exponentially decreasing space density (EDSD) before the distance (C. Bailer-Jones et al. 2018),

$$P(r|L) = \begin{cases} \frac{1}{2L^3} r^2 \exp\left(-\frac{r}{L}\right) & \text{if } r > 0 \\ 0 & \text{otherwise} \end{cases} \quad (5)$$

where $L > 0$ is a length scale. The prior shows a single peak at $2L$, and L changes based on Galactic longitude (l) and latitude (b). According to the model, which accounts for expected variations in the distribution of stellar distances in the *Gaia*-observed Galaxy (C. Bailer-Jones et al. 2018).

$$P^*(r|\overline{\omega}, \sigma_{\overline{\omega}}, L_{\rm sph}(l,b)) = \begin{cases} r^2 \exp\left[-\frac{r}{L_{\rm sph}(l,b)} - \frac{1}{2\sigma_{\overline{\omega}}^2}\left(\overline{\omega} - \overline{\omega}_{zp} - \frac{1}{r}\right)^2\right] & \text{if } r > 0 \\ 0 & \text{otherwise} \end{cases} \quad (6)$$

For a star's actual distance r, the parallax is $1/r$, with the measured parallax ($\bar{\omega}$) subject to observational noise of $1/r$. By considering the Gaussian likelihood of the parallax ($\bar{\omega}$) with a standard deviation ($\sigma_{\bar{\omega}}$) and using the EDSD prior from equation (5), we can obtain the unnormalized posterior over the distance to a source (C. Bailer-Jones et al. 2018). The three physical parameters – finite parallax ($\bar{\omega}$), positive standard deviation ($\sigma_{\bar{\omega}}$), and positive scale length Lsph – ensure a proper (i.e. normalizable) density function (C. Bailer-Jones et al. 2018). The accuracy of parallax measurements is limited, especially for distant stars, due to the precision of fractional values. C. Bailer-Jones et al. (2018) opted to estimate distances without assuming specific properties of individual stars or the level of

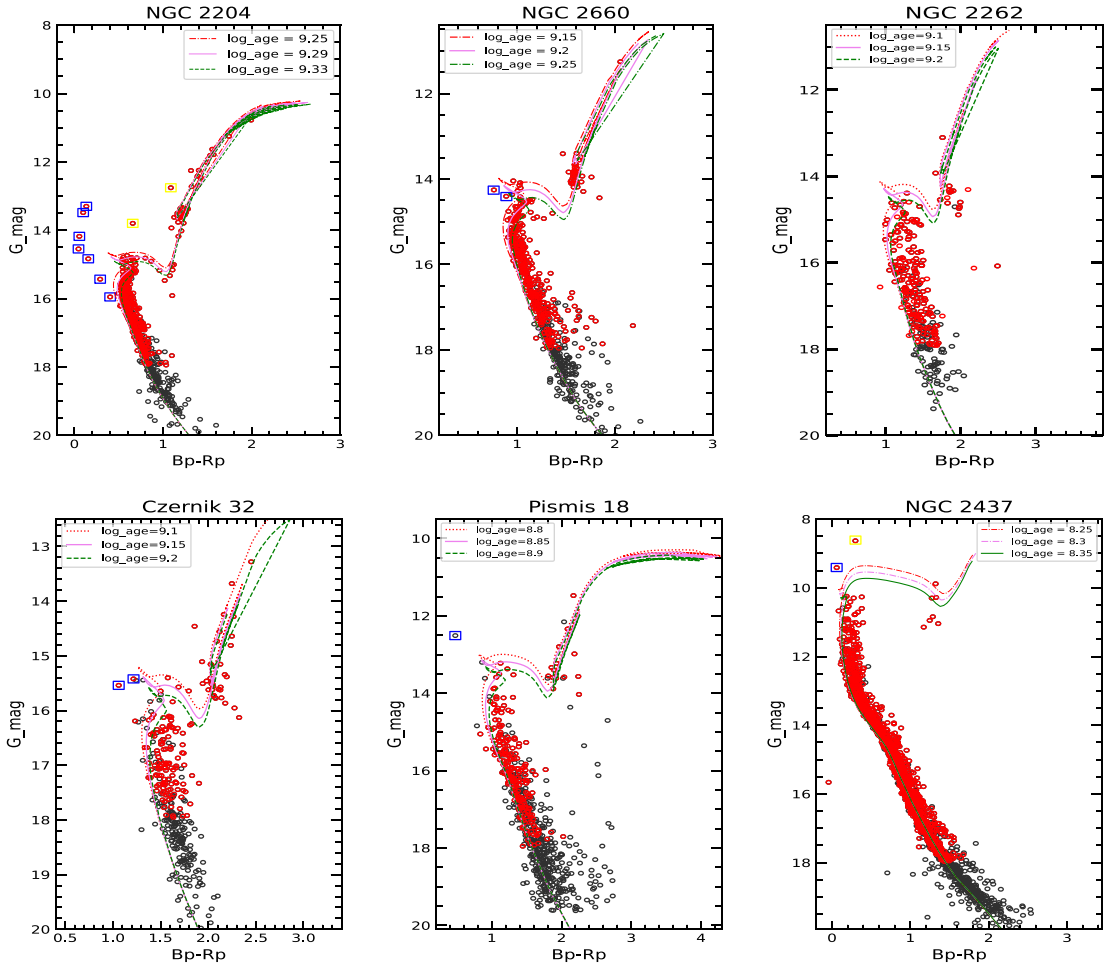

Figure 8. The *Gaia* DR3 colour–magnitude diagram of the studied cluster displays isochrones for the log age values indicated in the plot legend based on models from P. Marigo et al. (2017). Black circles represent the probable cluster members identified in this study, while red circles denote stars matched with the T. Cantat-Gaudin et al. (2020) catalogue. Blue and yellow squares mark the blue straggler stars (BSSs) and yellow straggler stars (YSSs), respectively, which were matched with the M. Rain et al. (2021) catalogue.

extinction affecting them. Following this method, we estimated the distance to each cluster by first applying a zero-point offset of −0.021 mas to the parallax values, as suggested by M. Groenewegen (2021). We then used Gaussian curve fitting to determine the mean and standard deviation of the parallax distribution for each cluster. The calculated distance values are as follows: for NGC 2204, $4.20^{+0.75}_{-0.56}$; for NGC 2660, $2.95^{+0.50}_{-0.67}$; for NGC 2262, $3.29^{+0.51}_{-0.39}$; for Czernik 32, $4.02^{+0.34}_{-0.30}$; for Pismis 18, $2.91^{+0.56}_{-0.79}$; and for NGC 2437, $1.76^{+0.74}_{-0.40}$ kpc. Table 1 shows the values of parallaxes. Our estimated values show fair agreement with T. Cantat-Gaudin et al. (2020) and W. S. Dias et al. (2021).

6 COLOUR–MAGNITUDE DIAGRAM ANALYSIS AND CLUSTER CHARACTERIZATION

The CMDs demonstrate the relationship between the surface temperature and absolute magnitude of stars, highlighting the corresponding colours and evolutionary tracks of stars with different initial masses in the cluster. Analysing the morphology of CMDs reveals key features, such as the main sequence, the turn-off point, and giant stars, which are crucial for deriving model-based estimates of the mass, age, and distance of each star (D. Bisht et al. 2019).

The interstellar reddening for each cluster was quantified by determining the colour excess $E(G_{BP} - G_{RP})$ through isochrone fitting to the observed CMD. This method enabled us to estimate the colour shift caused by interstellar dust extinction. The derived values of $E(G_{BP} - G_{RP})$ range from 0.14 to 0.80. To estimate the extinction in the *Gaia* G band, we applied the empirical relation $A_G = 1.86 \times E(G_{BP} - G_{RP})$, as given by L. Casagrande & D. A. VandenBerg (2018), resulting in A_G values between 0.80 and 1.35 mag. The corresponding colour excess in the Johnson system, $E(B - V)$, was derived using the transformation equation $E(B - V) = 0.72 \times E(G_{BP} - G_{RP})$, yielding values in the range 0.15–0.58. Using the computed values of A_G and $E(B - V)$, the extinction ratio $R_G = A_G/E(B - V)$ was calculated for each cluster. The derived values of R_G are 2.47 for NGC 2204, 2.45 for NGC 2660, 2.56 for NGC 2262, 2.55 for Cz 32, 2.53 for Pismis 18, 2.57 for NGC 2437. These results were compared with the standard extinction ratio $R_G \approx 2.74$ reported by L. Casagrande & D. A. VandenBerg (2018), suggesting that the extinction towards these clusters follows the typical interstellar reddening law, with no significant anomalies in the dust properties along their lines of sight. In this study, the distances obtained from *Gaia* parallax measurements were used as fixed inputs during the isochrone fitting process, as shown in Fig. 8. We did not treat distance as a free parameter in the fitting. Instead,

Table 3. Comparison of derived cluster parameters from this study with those reported in the literature for the six open clusters analysed.

Author	$\mu_\alpha cos(\delta)$ mas yr^{-1}	μ_δ mas yr^{-1}	Parallax mas	d_{plx} (kpc)	Age (Gyr)	R_{GC} (kpc)	X_{GAL} (kpc)	Y_{GAL} (kpc)	Z_{GAL} (kpc)
				NGC 2204					
This study	-0.58 ± 0.07	1.96 ± 0.12	0.202 ± 0.07	$4.20^{+0.75}_{0.56}$	1.950 ± 0.18	11.678 ± 0.302	-2.801 ± 0.234	-2.905 ± 0.324	-1.168 ± 0.223
T. Cantat-Gaudin et al. (2020)	-0.560	1.96	0.21	3.991	2.089	11.344	-2.663	-2.759	-1.107
M. Angelo et al. (2023)	-0.57 ± 0.06	1.95 ± 0.05	–	–	1.995 ± 0.230	11.1 ± 0.50	–	–	–
W. S. Dias et al. (2021)	-0.56 ± 0.14	1.98 ± 0.15	0.212 ± 0.07	4.11 ± 0.12	2.090 ± 0.144	–	–	–	–
				NGC 2660					
This study	-2.74 ± 0.20	5.20 ± 0.27	0.33 ± 0.10	$2.95^{+0.50}_{-0.67}$	1.585 ± 0.183	9.192 ± 0.528	-0.209 ± 0.120	-2.932 ± 0.288	-0.155 ± 0.219
T. Cantat-Gaudin et al. (2020)	-2.76	5.17	0.31	2.788	0.933	8.978	-0.197	-2.777	-0.146
W. S. Dias et al. (2021)	-2.74 ± 0.14	5.17 ± 0.16	0.31 ± 0.06	2.640 ± 0.11	1.202 ± 0.195	–	–	–	–
				NGC 2262					
This study	0.30 ± 0.11	0.11 ± 0.10	0.26 ± 0.11	$3.29^{+0.51}_{-0.39}$	1.413 ± 0.163	11.454 ± 0.442	-2.831 ± 0.332	-1.672 ± 0.225	-0.122 ± 0.229
G. Carraro et al. (2005)	–	–	–	3.6	1.000 ± 0.2	11.7	-1.8	3.1	-0.13
T. Cantat-Gaudin et al. (2020)	0.26	0.11	0.22	3.552	0.646	11.539	-3.056	-1.805	-0.130
W. S. Dias et al. (2021)	0.29 ± 0.18	0.11 ± 0.16	0.23 ± 0.11	2.91 ± 0.18	1.023 ± 0.118	–	–	–	–
				Czernik 32					
This study	-2.96 ± 0.18	2.48 ± 0.15	0.22 ± 0.12	$4.02^{+0.34}_{-0.30}$	1.413 ± 0.163	10.784 ± 0.524	-1.641 ± 0.256	-3.668 ± 0.645	-0.122 ± 0.211
G. Carraro et al. (2005)				4.1	1.000 ± 0.3	10.8	-1.7	3.7	-0.12
T. Cantat-Gaudin et al. (2020)	-2.96	2.48	0.196	4.139	1.122	10.717	-1.690	-3.777	-0.125
E. Bica & C. Bonatto (2005)	–	–	–	4.0 ± 0.2	1.120 ± 200	10.3 ± 0.3	–	–	-0.121 ± 0.08
W. S. Dias et al. (2021)	-2.96 ± 0.12	2.47 ± 0.12	0.194 ± 0.06	3.67 ± 0.21	1.349 ± 0.124	–	–	–	–
				Pismis 18					
This study	-5.69 ± 0.22	-2.35 ± 0.21	0.353 ± 0.10	$2.91^{+0.56}_{-0.79}$	0.708 ± 0.082	7.079 ± 0.542	1.799 ± 0.520	-2.284 ± 0.421	0.016 ± 0.394
T. Cantat-Gaudin et al. (2020)	-5.66	-2.29	0.332	2.860	0.575	6.943	1.770	-2.247	0.015
D. Hatzidimitriou et al. (2019)	-5.65 ± 0.08	-2.29 ± 0.11	0.335 ± 0.054	2.47	0.700	6.800	–	–	–
W. S. Dias et al. (2021)	-5.67 ± 0.11	-2.29 ± 0.12	0.328 ± 0.07	2.19 ± 0.08	0.676 ± 0.078	–	–	–	–
				NGC 2437					
This study	-3.87 ± 0.18	0.41 ± 0.19	0.60 ± 0.07	$1.76^{+0.74}_{-0.40}$	0.199 ± 0.046	9.682 ± 0.340	-1.083 ± 0.422	-1.381 ± 0.198	0.124 ± 0.050
T. Cantat-Gaudin et al. (2020)	-3.83	0.36	0.603	1.511	0.302	9.345	-0.930	-1.185	0.106

the primary objective was to estimate the interstellar reddening and the ages of the clusters by fitting theoretical isochrones from P. Marigo et al. (2017) to the *Gaia G* versus $(G_{BP} - G_{RP})$ CMDs. We determined the metallicities of the clusters through theoretical isochrone fitting. The obtained values are 0.006 ± 0.004 (NGC 2204), 0.010 ± 0.003 (NGC 2660), 0.010 ± 0.003 (NGC 2262 and Czernik 32), 0.020 ± 0.004 (Pismis 18), and 0.017 ± 0.003 (NGC 2437), respectively. They show that some clusters are close to solar metallicity ($Z_\odot \approx 0.0142$; M. Asplund et al. 2009), while others exhibit slightly sub-solar values. The modest differences correlate with the clusters' Galactocentric radii. This pattern aligns with the well-established radial metallicity gradient of the Galactic disc (e.g. E. Friel 1995; M. Netopil et al. 2016). In particular, the sub-solar metallicities of NGC 2204, NGC 2262, and Czernik 32 are consistent with their older ages and larger Galactocentric distances. The near-solar values of Pismis 18 and NGC 2437 reflect their positions closer to the Galactic centre. For NGC 2204, we cross-matched our member stars with the Apache Point Observatory Galactic Evolution Experiment (APOGEE) data set. We identified 27 stars with available metallicities, obtaining a mean value of [Fe/H] $= -0.26 \pm 0.04$ ($Z = 0.007 \pm 0.0008$). This is broadly consistent with the high-resolution spectroscopic study of B. J. Anthony-Twarog et al. (2024), who reported [Fe/H] $= -0.40 \pm 0.12$ ($Z = 0.005 \pm 0.002$) based on 45 stars. For NGC 2660 and Pismis 18, L. Magrini et al. (2023) derived [Fe/H] $= -0.05$ ($Z = 0.012$) and $+0.14$ ($Z = 0.0193$), respectively, from *Gaia*–ESO survey data. For NGC 2437, T. Davidge (2013) adopted a metallicity of $Z = 0.019$, while for NGC 2262 and Czernik 32, G. Carraro et al. (2005) assumed $Z = 0.008$ in their isochrone-based analysis. Overall, these spectroscopic and literature values are in good agreement with our isochrone-based estimates, further supporting the robustness of our metallicity determinations.

The derived ages for the clusters span from 0.199 to 1.95 Gyr. The isochrone fitting results, including the estimated ages and distances for each cluster, are summarized in Table 3. To assess the reliability of our fits, we applied the reduced chi-square test for isochrone fitting, following the methodology outlined in G. Valle, M. Dell'Omodarme & E. Tognelli (2021) and D. Bisht et al. (2024), to determine the optimal values of the fitting parameters. The reduced chi-square (χ^2_r) is a widely used method for evaluating the goodness of fit, which quantifies how well the model (isochrone) describes the observed data. The optimal values of the distance modulus and colour were determined by minimizing the χ^2_r statistic, which compares the difference between the observed and fitted CMDs, considering the observational errors. The resulting minimized reduced chi-square values are 0.75 for NGC 2204, 0.70 for NGC 2660, 0.65 for NGC 2262, 0.59 for Czernik 32, 0.62 for Pismis 18, and 0.77 for NGC 2437. These values indicate that our fitting procedure is robust and appropriate for the data (L. Magrini et al. 2023).

BSSs are observed to be both brighter and bluer than the main-sequence turn-off, following an extension of the main sequence in the CMDs of star clusters (A. Sandage 1953). Their formation is primarily attributed to two mechanisms: mass transfer in binary systems (W. McCrea 1964) and direct stellar collisions (J. Hills & C. Day 1976). Additionally, recent studies suggest that BSSs may result from the merger of main-sequence stars within hierarchical triple systems, driven by the eccentric Kozai–Lidov mechanism (S. Naoz & D. C. Fabrycky 2014), which significantly contributes to BSS formation in OB associations. Extensive research has characterized BSS populations and explored their formation scenarios in open and globular clusters (F. R. Ferraro et al. 2009; A. K. Dattatrey et al. 2023; R. Yadav et al. 2024).

In this analysis, we identified both BSSs and YSSs, which are consistent with the findings of M. Rain et al. (2021) and V. V. Jadhav et al. (2021). Specifically, we detected seven BSSs and two YSSs in NGC 2204, two BSSs in NGC 2660, two BSSs in Czernik 32, and one BSS along with one YSS in NGC 2437.

The matched stars are highlighted in Fig. 8 using blue and yellow square boxes. Furthermore, our analysis uncovered one previously unreported BSS in Pismis 18, marked with blue square boxes in the Fig. 8.

In NGC 2204, we identified five BSSs within a radius of 5 arcmin from the cluster centre, while the remaining two are located at distances of 7 and 11 arcmin. Additionally, two YSSs are positioned at 1.83 and 4.27 arcmin from the centre. In NGC 2660, two BSSs are situated within the core radius of the cluster. For NGC 2437, one BSS is found at a distance of 9 arcmin from the centre, while one YSS is located 5.9 arcmin away. In Czernik 32, we detected two BSSs at distances of 2.17 and 4.3 arcmin from the cluster centre. In Pismis 18, one newly identified BSS is located 7.2 arcmin from the cluster centre. All BSS identified in this study have a membership probability exceeding 90 per cent. The possible formation mechanisms suggest that the five BSSs in the core region of NGC 2204 likely formed through stellar collisions, while the two BSS in the halo region were probably formed via mass transfer in binary systems (M. Mapelli et al. 2006). In general, the higher stellar density in the central region of a cluster makes the collisional channel more favourable there, while the lower-density halo environment is more conducive to binary evolution pathways. Nevertheless, we note that location alone is not definitive, as dynamical interactions and mass segregation can alter the positions of BSSs. Further spectroscopy or spectral energy distribution (SED) analysis will be necessary to distinguish formation mechanisms.

We have determined the Galactocentric coordinates of the clusters (X_{GAL}, Y_{GAL}, Z_{GAL}) and estimated their Galactocentric distance (R_{GC}), as listed in Table 3. The five clusters are located close to the Galactic plane, with their vertical distances ranging from −0.155 to 0.124 kpc. The remaining cluster is positioned farther from the plane, at −1.168 kpc below the Galactic plane. The calculated parameters show good agreement with the values reported by T. Cantat-Gaudin et al. (2020). This information is crucial for understanding the cluster's environment, its motion within the Galaxy, and its interactions with other Galactic components. Furthermore, Galactocentric coordinates serve as a foundation for broader astrophysical studies, contributing to a deeper understanding of the cluster's role in the dynamic structure of the Milky Way.

7 DYNAMICAL STUDY

To study the luminosity function (LF) and mass function (MF), the first crucial step is to eliminate field star contamination from the sample of stars in the cluster region. A statistical field star subtraction method is employed, assuming that field stars in the cluster and surrounding areas have a similar distribution (R. Sagar & W. Griffiths 1998) and (R. L. Phelps & K. A. Janes 1993).

7.1 Luminosity function

The LF represents the distribution of stars in a cluster based on their luminosity. For main-sequence stars in each cluster, the LF is derived from the true cluster stars identified in Section 3. To construct the LFs histogram, we used the stars from the CMDs (G versus $G_{BP} - G_{RP}$) as targets. The apparent G magnitudes of the cluster stars were converted into absolute magnitudes using the distance modulus and A_G (extinction in the G band). A binning interval of 1 mag was chosen to ensure a sufficient number of stars for good statistical analysis. The constructed histogram is illustrated in the Fig. 9. The mean absolute magnitudes were found to be 4.3, 5.3, 4.8, 4.5, 5.5, and 5.8 for NGC 2204, NGC 2660, NGC 2262, Czernik 32, Pismis 18, and NGC 2437, respectively. These values represent the central tendency of the luminosity function for the main-sequence members in each cluster. Building upon this, we next examine the mass function, which provides a deeper understanding of the stellar mass distribution and the dynamic state of each cluster.

7.2 Mass function

The mass function (MF) describes the distribution of stellar masses within a cluster per unit volume. To derive the MF, the observed LF is converted using a mass–luminosity relation that depends on the cluster's fundamental parameters, such as reddening, distance, and age. For this purpose, we employed theoretical isochrones from P. Marigo et al. (2017). The observed stars were grouped into magnitude bins, and each bin was associated with a corresponding mass interval derived from the adopted isochrone. This enabled the transformation of the LF into the MF. The resulting mass function plots are shown in Fig. 10. The slope of the resulting MF was determined by fitting a power law to the mass distribution of cluster members using a least-squares fitting approach, as described by equation (7)

$$log\frac{dN}{dM} = -(1+x) \times log(M) + constant \quad (7)$$

dN represents the number of stars within a specific mass bin dM, while M denotes the central mass of that bin. The slope of the MFs, x, can be derived from the equation mentioned earlier. We calculate the MFs slope for three distinct regions of each cluster: the core, the halo, and the entire cluster region. The radius values for these cluster regions are referenced from Section 4.

We calculated the MF slopes for the stellar populations in each cluster, with values ranging from 0.36 to 0.97 in the core regions, 1.35 to 1.61 in the haloes, and 0.96 to 1.19 for the entire clusters. The total stellar masses of the clusters range between 268 $M_\odot$ and 2453 $M_\odot$, where NGC 2262 is the least massive, and NGC 2437 is the most massive cluster in our sample. On average, the typical stellar mass across all clusters is close to 1 $M_\odot$, reflecting the dominance of low- and intermediate-mass main-sequence stars in these OCs. The stellar mass ranges adopted for the mass function calculations are as follows: 1.58–0.56 $M_\odot$ for NGC 2204, 1.61–0.60 $M_\odot$ for NGC 2660, 1.94–0.56 $M_\odot$ for NGC 2262, 1.93–0.61 $M_\odot$ for Czernik 32, 2.63–0.60 $M_\odot$ for Pismis 18, and 3.97–0.60 $M_\odot$ for NGC 2437. These ranges and mass-function related parameters listed in Table 4 were derived from the isochrone-based mass–luminosity relations of the member stars.

The MF slopes are shallower in the core region, whereas in the entire cluster region, it is slightly lower than the Salpeter value of x = 1.354 (E. E. Salpeter 1955). In contrast, the halo region shows good agreement with the Salpeter value. Moreover, the MF slopes tend to increase towards the outer regions of the cluster compared to the core. This trend may be a result of the concentration of massive stars in the cluster core. In contrast, low stars migrate toward the halo and outer regions, indicating possible mass segregation, as discussed in the next section.

7.3 Mass segregation

In the study of mass segregation, it is suggested that high-mass stars migrate toward the cluster centre while low-mass stars shift toward the halo region. This phenomenon has been observed in various clusters by several authors, including P. Kroupa & C. M.

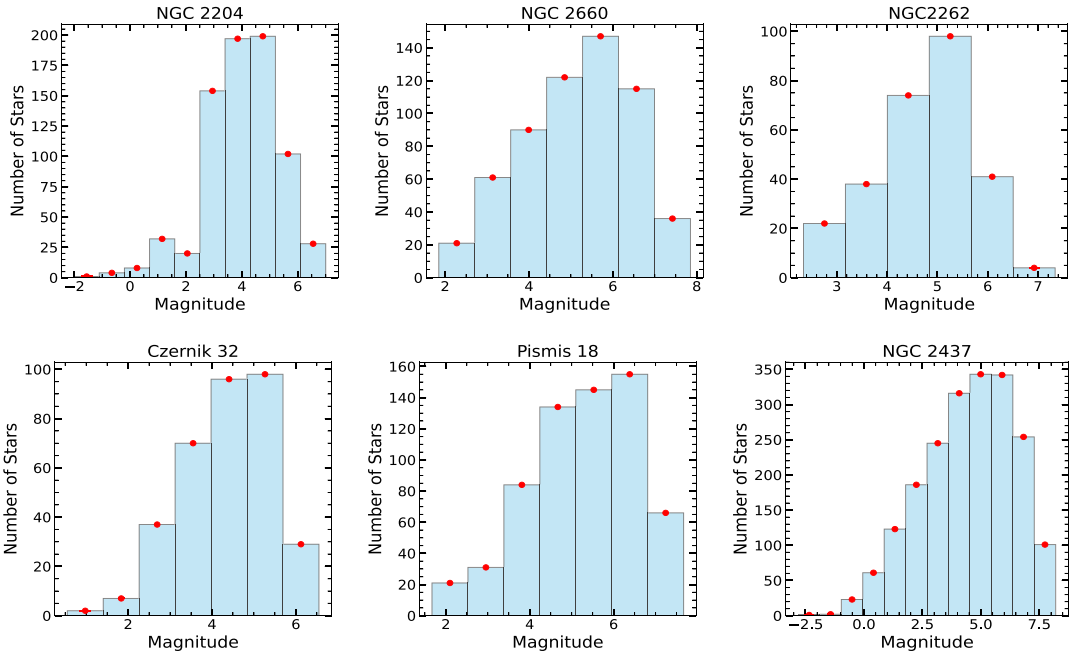

Figure 9. Histograms show the luminosity distribution of stars in each open cluster as a function of absolute magnitude. The blue bars represent the number of stars in each magnitude bin, and the red dots indicate the corresponding Poisson uncertainties.

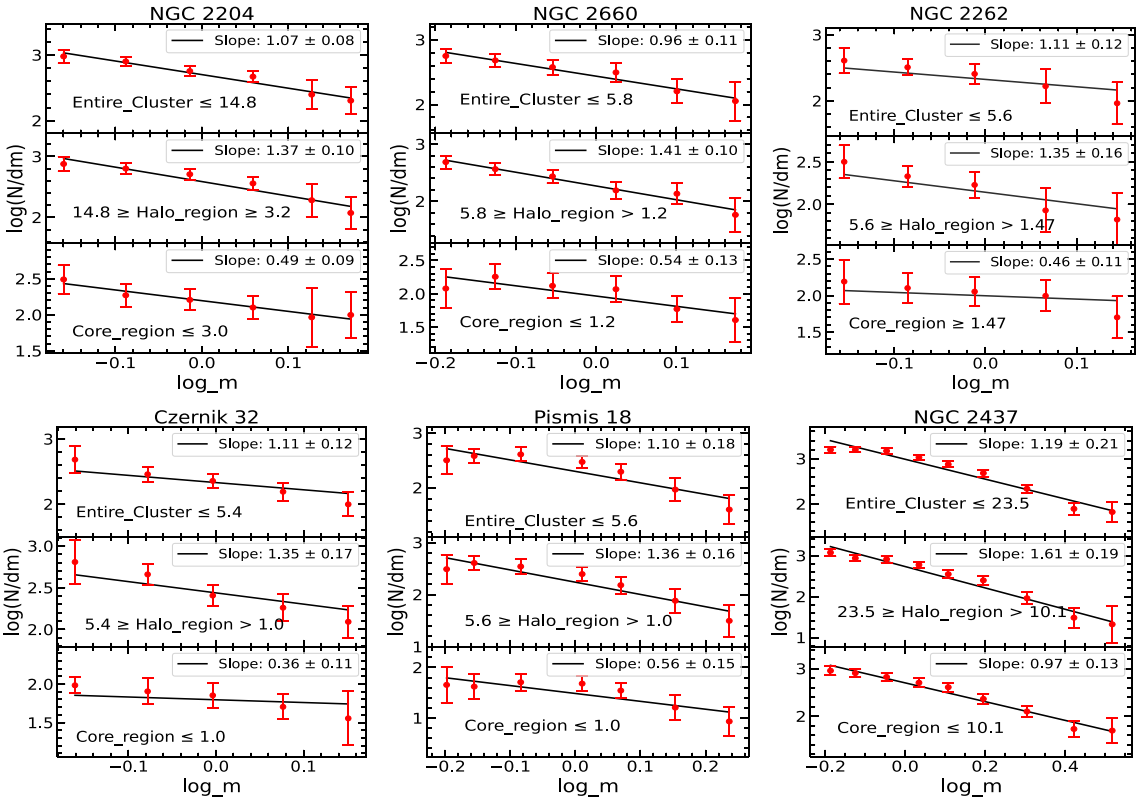

Figure 10. Mass function (MF) slopes for the six open clusters – NGC 2204, NGC 2660, NGC 2262, Czernik 32, Pismis 18, and NGC 2437 – evaluated separately for the entire cluster region, halo region, and core region. The MF slope (x) is derived by applying a least-squares linear fit to the $\log(N/\Delta \log m)$ versus $\log m$ distribution, shown as solid black lines in each panel. Error bars represent Poisson uncertainties. Variations in the MF slopes across different regions provide insights into the internal dynamical evolution and degree of mass segregation within each cluster.

Table 4. The mass-function slopes for each region, along with the total mass, mean mass, relaxation time, and half-mass radius values for each cluster in this study.

Cluster	Mass Range $M_\odot$	Mass function slope (x) Core	Halo	Entire region	Total mass $M_\odot$	$\bar{m}$ $M_\odot$	R_h Parcsec	T_R Myr
NGC 2204	1.58–0.56	0.49 ± 0.09	1.37 ± 0.10	1.07 ± 0.08	682 ± 80	0.91	4.26 ± 0.25	90.1 ± 8.1
NGC 2660	1.61–0.60	0.54 ± 0.13	1.41 ± 0.12	0.96 ± 0.11	566 ± 60	0.96	1.73 ± 0.28	21.1 ± 5.4
NGC 2262	1.94–0.56	0.46 ± 0.11	1.35 ± 0.16	1.11 ± 0.12	268 ± 40	0.95	1.93 ± 0.34	19.9 ± 5.5
Czernik 32	1.93–0.61	0.36 ± 0.09	1.35 ± 0.17	1.11 ± 0.12	351 ± 50	1.03	1.79 ± 0.30	18.1 ± 4.8
Pismis 18	2.63–0.60	0.56 ± 0.15	1.36 ± 0.16	1.10 ± 0.18	763 ± 110	1.19	1.54 ± 0.20	16.4 ± 3.3
NGC 2437	3.97–0.60	0.97 ± 0.13	1.61 ± 0.19	1.19 ± 0.21	2453 ± 220	1.23	6.17 ± 0.30	188.7 ± 15.8

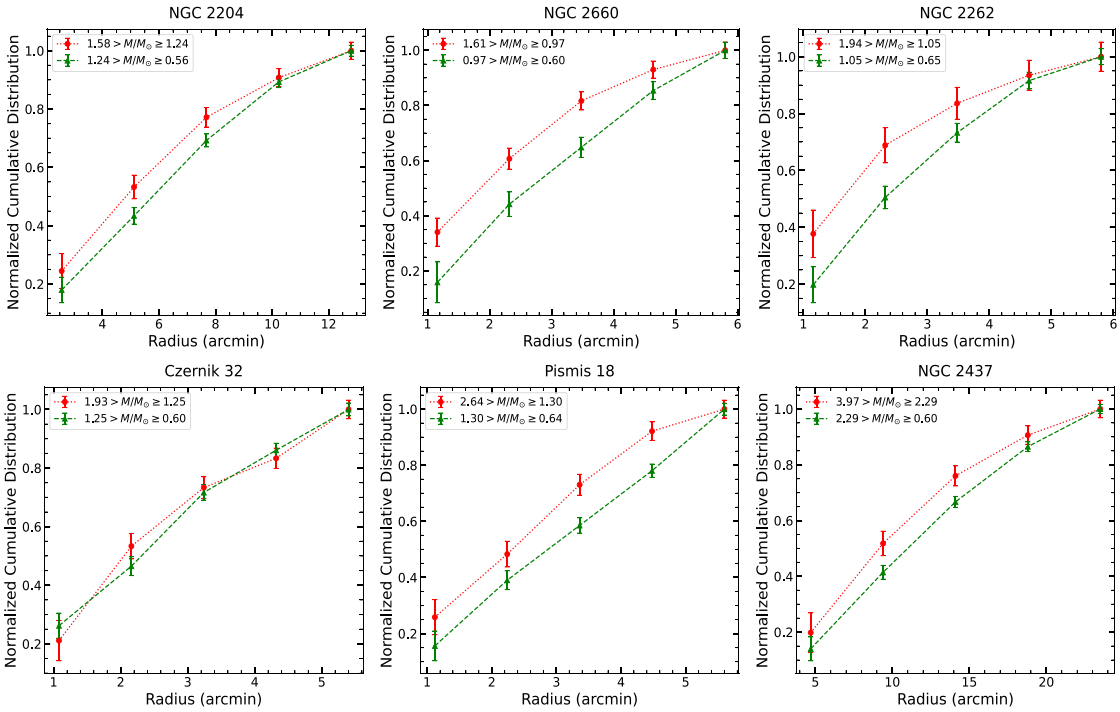

Figure 11. Cumulative radial distribution of stars in different mass ranges for six open clusters: NGC 2204, NGC 2660, NGC 2262, Czernik 32, Pismis 18, and NGC 2437. The red and green dashed lines represent the high-mass and low-mass stellar populations, respectively, with the specific mass ranges indicated in the legend of each panel. A steeper distribution of high-mass stars towards the centre suggests evidence of mass segregation in these clusters.

Boily (2002), S. Dib, J. Kim & M. Shadmehri (2007), and D. Bisht et al. (2020, 2022a). This occurs due to the equipartition of energy: high-mass stars, which have lower velocities and experience stronger gravitational forces, concentrate near the cluster centre. Conversely, low-mass stars with higher velocities can more easily escape the gravitational pull of the central region, resulting in their distribution towards the cluster's outskirts. In this analysis, we used only true cluster members to investigate the effect of mass segregation. To analyse mass segregation in different stellar regimes, the stars in each cluster were divided into two mass bins: high-mass and low-mass stars. The mass ranges for each bin were defined as follows: NGC 2204 ($1.58 > M/M_\odot \geq 1.24$ and $1.24 > M/M_\odot \geq 0.56$), NGC 2660 ($1.61 > M/M_\odot \geq 0.97$ and $0.97 > M/M_\odot \geq 0.60$), NGC 2262 ($1.94 > M/M_\odot \geq 1.05$ and $1.05 > M/M_\odot \geq 0.65$), Czernik 32 ($1.93 > M/M_\odot \geq 1.25$ and $1.25 > M/M_\odot \geq 0.60$), Pismis 18 ($2.64 > M/M_\odot \geq 1.30$ and $1.30 > M/M_\odot \geq 0.64$), and NGC 2437 ($3.97 > M/M_\odot \geq 2.29$ and $2.29 > M/M_\odot \geq 0.60$). These bins were chosen to capture the stellar distribution above and below the median mass range of each cluster's main-sequence population.

Fig. 11 shows the cumulative radial distribution of cluster members for all clusters. We performed the Kolmogorov–Smirnov (K–S) test, a non-parametric statistical method, to evaluate the statistical significance of the mass-segregation effect. This test compares the cumulative distribution functions (CDFs) of two independent samples to determine whether they originate from the same distribution. Our analysis measures the maximum difference between the empirical CDFs of more massive and less massive stars. A significant result indicates a substantial difference in their spatial distributions, suggesting the presence of mass segregation within the cluster. This enables us to evaluate how stellar dynamics impact the arrangement of stars based on their masses. Our analysis yielded P-values ranging from 0.10 to 0.01, corresponding to confidence levels between 90 per cent and 99 per cent. These results provide statistically significant evidence that the spatial distributions of high- and low-mass stars differ across all six clusters. Such a trend strongly supports the presence of mass segregation, a dynamic process wherein more massive stars migrate towards the cluster centre over time due to two-body relaxation effects.

Table 5. The orbital parameters of the clusters under study. Here, (R, Z) are the position coordinates, and (U, V, W) are the velocity components of the clusters. R_{ap} and R_{peri} are the apogalactic and perigalactic positions in the orbits of the cluster. Z_{max} is the maximum distance travelled by the cluster from the Galactic disc, and T is the time of the revolution.

Name	R (kpc)	Z (kpc)	U (km s^{-1})	V (km s^{-1})	W (km s^{-1})	Eccentricity	R_{ap} (kpc)	R_{peri} (kpc)	Z_{max} (kpc)	T (Myr)
NGC 2204	11.19	−1.14	80.58	195.42	−13.17	0.10	12.50	10.21	1.32	0.25
NGC 2660	08.72	−0.13	71.33	214.65	20.88	0.05	09.61	08.69	0.41	0.19
NGC 2262	10.96	−0.09	43.73	199.07	10.12	0.06	11.17	09.81	0.24	0.23
Czernik 32	10.32	−0.10	80.75	194.99	−19.71	0.02	10.46	9.95	0.45	0.22
Pismis 18	06.61	0.03	69.34	200.23	−10.82	0.06	6.62	5.90	0.12	0.12
NGC 2437	9.19	0.15	32.72	206.95	−15.93	0.03	9.19	8.57	0.32	0.19

7.4 Relaxation time

The relaxation time provides a meaningful measure of the time-scale over which a cluster loses any remnants of its initial conditions and reaches energy equipartition. It is characterized as the time when the stellar velocity distribution becomes Maxwellian. L. Spitzer Jr & M. H. Hart (1971) define the relaxation time T_R using the following equation:

$$T_R = \frac{8.9 \times 10^5 \sqrt{N} \times R_h^{3/2}}{\sqrt{\bar{m}} \times log(0.4N)}. \quad (8)$$

N is the number of stars with a membership probability greater than 70 per cent. $\bar{m}$ represents the average mass of the cluster stars in solar units, and R_h denotes the half-mass radius in parsecs, as shown in Table 4. R_h specifically indicates the radius at which the cluster mass is half of the total cluster mass.

We have derived the value R_h based on the transformation equation as given in I. Šablevičiūtė (2006)

$$R_h = 0.547 \times R_c \times \left(\frac{R_t}{R_c}\right)^{0.486}.$$

Where R_c is the core radius and R_t is the tidal radius, values mentioned in the Table 2. The half-mass radius (R_h) ranges from 1.54 to 6.17 parsec, as presented in Table 4. Similarly, the estimated relaxation time (T_R) varies from 16 to 189 Myr, as shown in the same table. Since the age of each cluster exceeds its corresponding relaxation time, all clusters are dynamically relaxed.

7.5 Orbits of the clusters

The orbital trajectories in the Galaxy were calculated for the six clusters under study using the GALPY module developed by J. Bovy (2015). The detailed method for deriving orbits of open clusters using GALPY is described in G. Rangwal et al. (2025). First, using ASTROPY, the heliocentric position and velocity components of all the OCs were transformed into their Galactocentric positions and velocities, which are listed in Table 5.

To perform an orbital analysis of clusters, we calculated the mean radial velocity (RV) using only the member stars of the cluster. For NGC 2204, we found 44 stars with RVs, yielding a mean value of 92.32 ± 2.29 km s^{-1}. For NGC 2660, 31 stars were identified with a mean RV of 22.66 ± 5.43 km s^{-1}. For NGC 2262, we found 13 stars with a mean RV of 63.94 ± 3.76 km s^{-1}. For Czernik 32, 15 stars were included, resulting in a mean RV of 72.29 ± 4.69 km s^{-1}. Pismis 18 had 22 stars with a mean RV of -24.70 ± 11.37 km s^{-1}. Finally, for NGC 2437, 156 stars were considered, with a corresponding mean RV of 45.15 ± 18.75 km s^{-1}.

For the present analysis, we also used **MWPotential2014** Galactic potential to derive the orbits. This axisymmetric Galactic potential consists of three main components: a power-law bulge with exponential cut-off, a Miyamoto–Nagai stellar disc, and a spherical Navarro–Frenk–White halo representing the dark matter. The model does not include non-axisymmetric features such as the Galactic bar or spiral arms; however, for OCs located in the thin disc at intermediate Galactocentric radii, this model provides a sufficiently accurate and widely used description of the Galactic potential. Since all clusters are located far from the central region of the galaxy, the influence of the Galactic bar will not be significant. The location of the Sun was taken at a distance of 8.178 kpc from the Galactic centre and velocity 220 km s^{-1} towards the Galactic rotation. The cluster orbits were back-integrated for a time interval equal to their age.

The calculated orbits are shown in Fig. 12, where the birth and present positions of these OCs are denoted by a red dot and a triangle, respectively. The trajectories shown in green represent the path of cluster motion in the RZ projection. Here, R is the distance of the cluster from the Galactic centre, and Z is the distance of the cluster from the Galactic disc. The purple trajectories represent the path followed by the cluster around the galactic centre in the projection of the x- and y-components of distance from the galactic centre. The calculated orbital parameters, such as eccentricity, apogalactic and perigalactic distance, maximum vertical distance travelled by the clusters from the Galactic disc, and the time period, are listed in Table 5.

We investigated the effect of uncertainties in the initial conditions, specifically proper motions, distance, and radial velocity on the derived orbital parameters using GALPY. Error propagation was performed through Monte Carlo sampling with 500 random realizations. In each realization, the input parameters were drawn from respective probability distributions, incorporating the observational uncertainties, and resulting orbits were integrated backward over 1.9 Gyr, corresponding to the ages of the oldest cluster in our sample. From the distribution of orbital solutions, we estimated the maximum standard deviation of 0.50 kpc in R, 0.05 kpc in Z, 19.43 km s^{-1} in U, 15.33 km s^{-1} in V 10.6 km s^{-1} in W, 0.05 in eccentricity, 1.13 kpc in R_{ap}, 1.02 kpc in R_{peri}, 0.31 in Z_{max}, and 0.02 Myr in T. This indicates that the uncertainties are relatively small compared to the orbital integration scale.

Fig. 12 shows that all the clusters under study are tracing a circular trajectory around the Galactic centre in a boxy pattern, a well-known characteristic of the thin disc Galactic clusters. The orbital analysis shows that all the clusters are born in the thin disc, hence moving very close to the Galactic disc, tracing a small vertical height. The oldest cluster of the sample, NGC 2204, is reaching the maximum vertical distance of 1.32 kpc, and all the other younger clusters are not reaching further than 0.45 kpc from the Galactic disc. This indicates that all these clusters are highly perturbed by the tidal forces present in the Galactic disc. This may be the reason for losing their low-mass stars in a short time duration, as indicated in the luminosity functions of these clusters shown in Fig. 9. NGC 2437 is the youngest cluster in

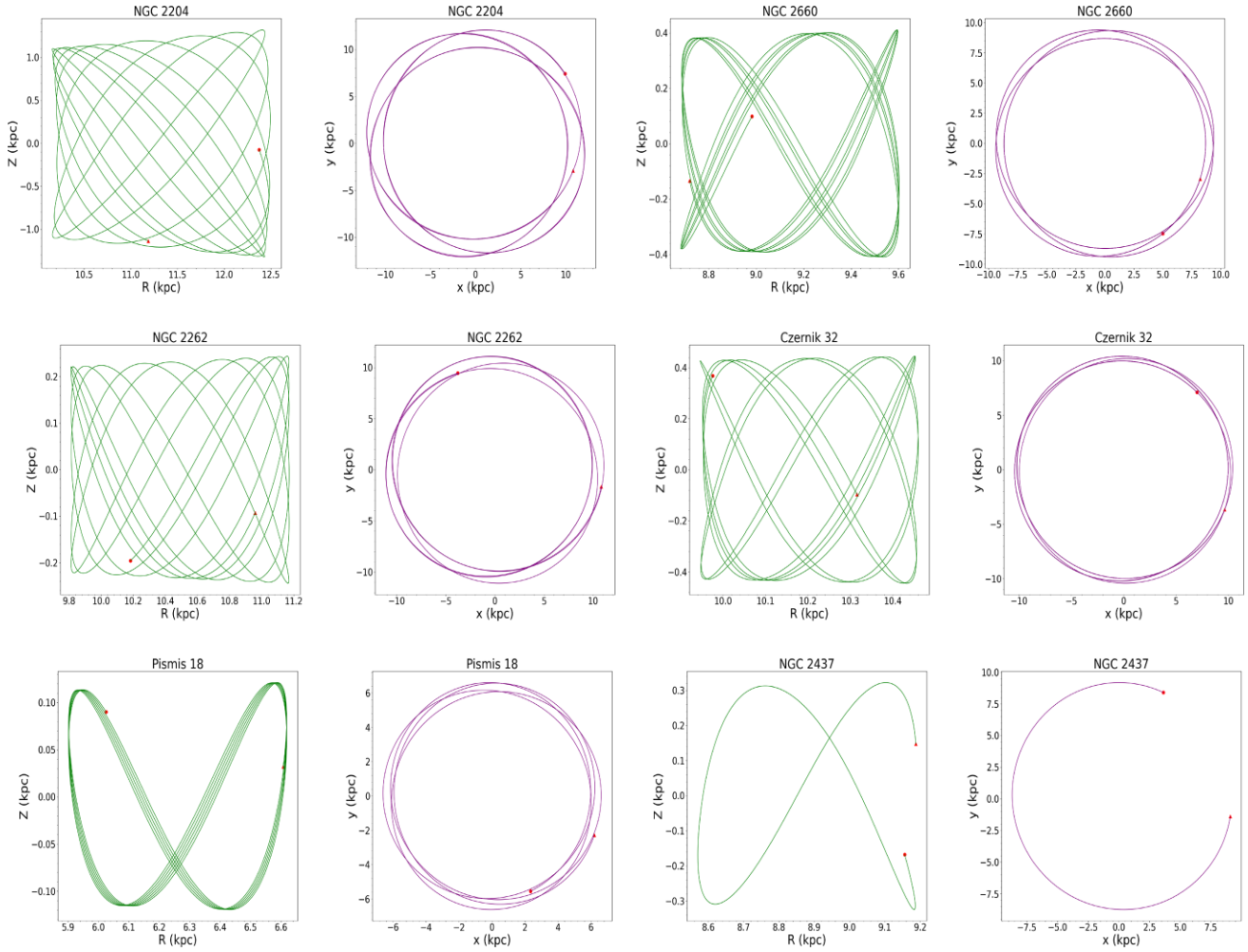

Figure 12. Orbital trajectories of the six open clusters under study – NGC 2204, NGC 2262, NGC 2660, Czernik 32, Pismis 18, and NGC 2437 – plotted in the XY, RZ, and YZ planes. These projections illustrate the Galactic orbits computed using the clusters' kinematic and positional parameters. Here, X and Y denote the positions in the Galactic plane relative to the Galactic centre, R is the radial distance from the Galactic centre, and Z is the vertical distance from the Galactic mid-plane. The red dot indicates the birth position, while the red triangle marks the present-day positions of the clusters. These orbital maps help trace the dynamical evolution and vertical oscillations of the clusters in the Galaxy.

the sample and has not completed one revolution around the Galactic centre. This is also the largest, with a radius of 23.5 arcmin, and the most populous cluster among all the clusters under study. The luminosity function suggests that low-mass stars have begun to evaporate, which may be attributed to their proximity to the Galactic disc.

8 IDENTIFICATION AND CLASSIFICATION OF VARIABLE STARS

Variable stars are celestial objects whose brightness changes over time, providing valuable insights into the physical processes that drive stellar evolution. In this study, we analysed *TESS* data to identify variable stars within the regions of the clusters NGC 2204, NGC 2262, Pismis 18, and NGC 2437.

We identified one variable star in NGC 2204 (TIC 59711686), one in NGC 2262 (TIC 369672843), and two variable stars in Pismis 18 (TIC 318 170 016 and TIC 318170024). In NGC 2437, eight variable stars were detected: TIC 94229743, TIC 94690694, TIC 94322635, TIC 94408904, TIC 94409484, TIC 94409620, TIC 94410959, and TIC 94519429. We analysed the light curves obtained from the *TESS* mission to investigate the variability characteristics of these stars. The periods were determined using the Lomb–Scargle algorithm (N. R. Lomb 1976; J. D. Scargle 1982), which is well-suited for analyzing unevenly spaced time-series data, as shown in the Figs 13 and 14. The estimated period and other parameters are shown in the Table 6.

The Hertzsprung–Russell (H–R) diagram primarily illustrates the empirical relationship between a star's spectral type and its luminosity. Alternative versions of the H–R diagram may plot temperature against luminosity or colour index versus absolute magnitude. The position of a star on the diagram is influenced not only by its initial mass and age but also by factors such as stellar winds, magnetic fields, rotation, and chemical composition. For variable stars, their location on the H–R diagram provides valuable insight into their evolutionary stage. Moreover, the H–R diagram has proven highly effective in classifying variable stars, as different types tend to occupy well-defined regions within it.

In the present study, we analysed the H–R diagram by plotting $\log(T_{\rm eff})$ versus $\log(L/L_{\odot})$ to determine the evolutionary stages of the identified variable stars. The effective temperature ($T_{\rm eff}$) and luminosity for seven stars were obtained from the Gaia Collaboration (2023). For an additional five member stars, the values of $\log(T_{\rm eff})$ and $\log(L/L_{\odot})$ were taken from the theoretical isochrone of P. Marigo

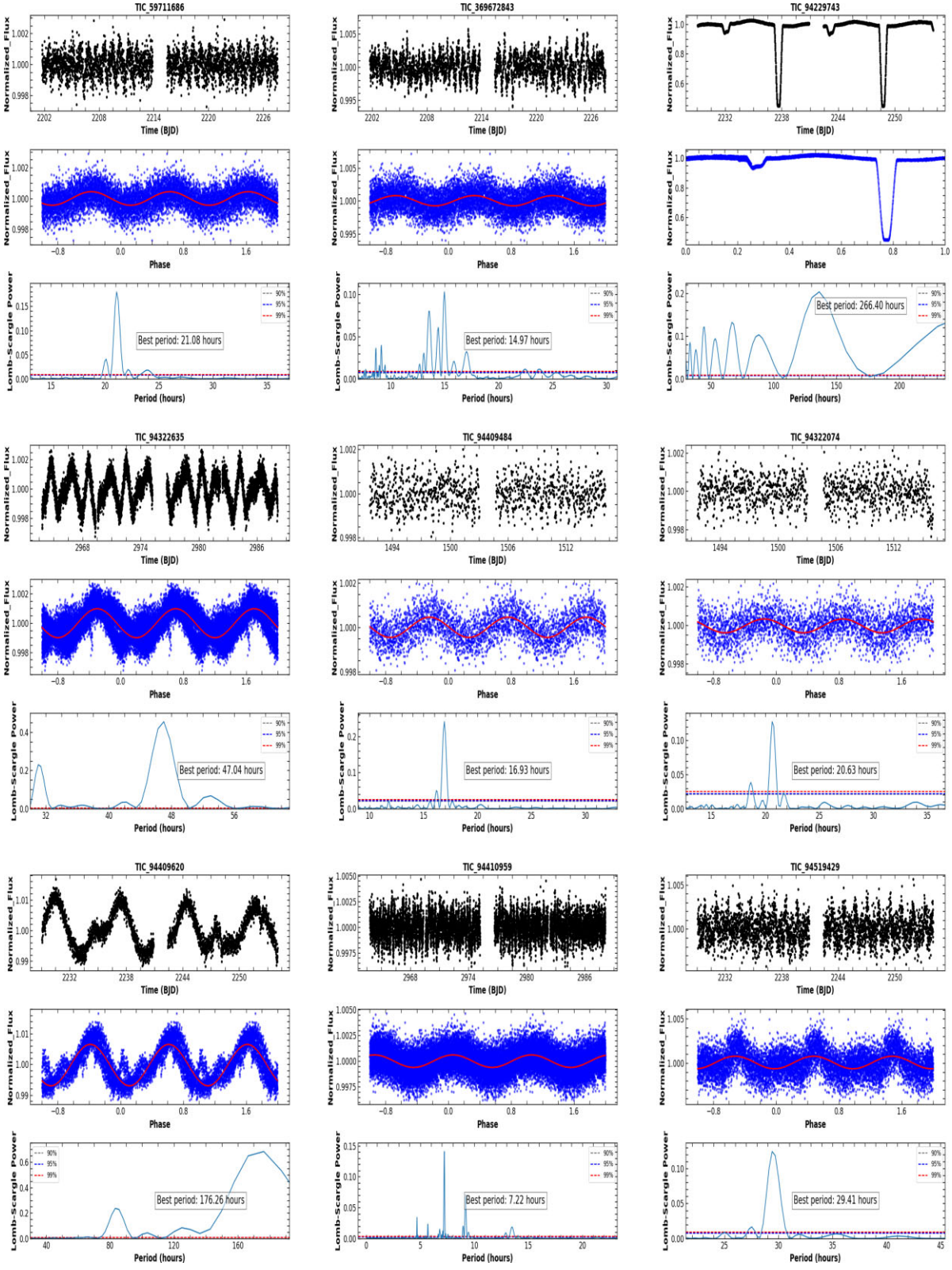

Figure 13. *– continued*

et al. (2017). The H–R diagram was constructed using these adopted values, as shown in Fig. 15. Two distinct theoretical instability strips, corresponding to slowly pulsating B-type (SPB) stars and γ Doradus stars, are also marked on the diagram. Within the instability strip corresponding to high-mass stars such as SPB stars, we identified one host star. Additionally, one variable star was found to lie within the γ Doradus instability strip. The positions of these variable stars on the H–R diagram have been used to classify their variability types.

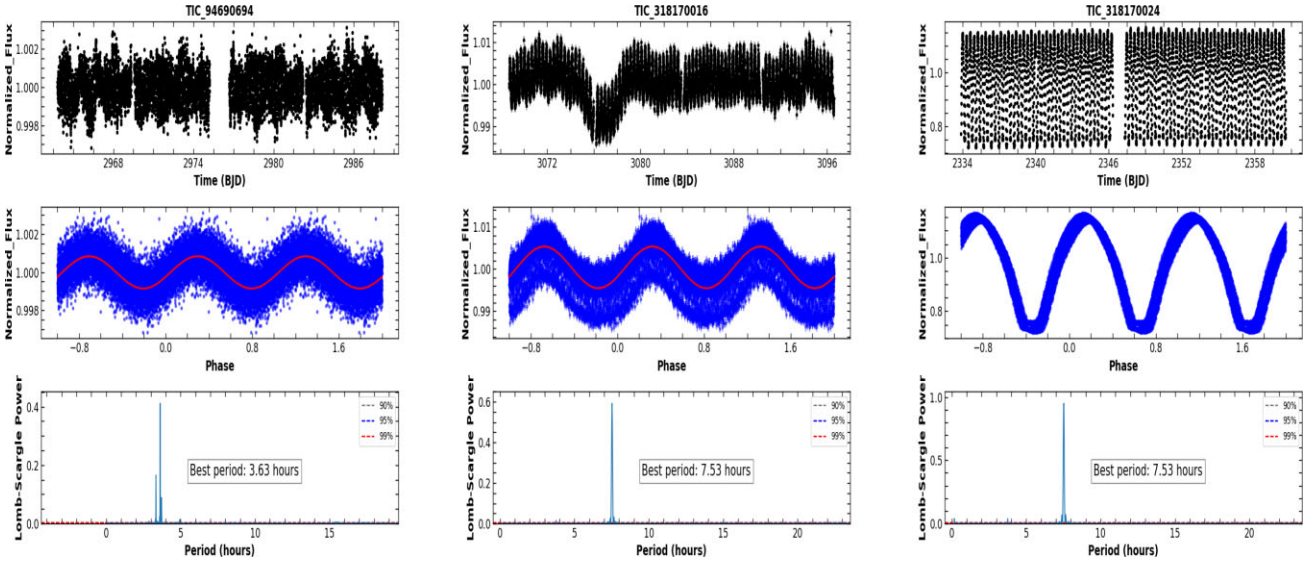

Figure 14. Light curves and periodogram analyses of the identified variable stars in the clusters NGC 2204, NGC 2262, Pismis 18, and NGC 2437. For each star, three plots are shown vertically: the observed *TESS* light curve (top), the phase-folded light curve with the fitted model overlaid in blue (middle), and the corresponding Lomb–Scargle periodogram (bottom). The panels correspond to the following stars (from top to bottom, left to right): TIC 59 711 686 (NGC 2204), TIC 369 672 843 (NGC 2262), TIC 318 170 024 and TIC 318 170 016 (Pismis 18), and TIC 94609694, TIC 94409620, TIC 94322635, TIC 94409484, TIC 94519429, TIC 94322074, and TIC 94 229 743 (NGC 2437). The detected periods, indicated by peaks in the periodograms, aid in classifying the variability types and provide constraints for stellar parameter estimation through light curve modelling.

Table 6. Basic parameters of the identified variable stars in the observed clusters. The columns list the TIC ID, right ascension (RA) and declination (Dec.) in J2000 coordinates, period (in hours), effective temperature ($T_{\rm eff}$ in K), membership status, and type of variability. Membership is denoted as 'M' for cluster members and 'F' for field stars. The variability types include γ Dor, SPB, and EW-type eclipsing binaries. The stars are grouped according to their respective clusters: NGC 2204, NGC 2262, Pismis 18, and NGC 2437.

ID	RA (J2000)	Dec. (J2000)	Period (h)	$T_{\rm eff}$ K	log ($T_{\rm eff}$) K	log(L/L$_\odot$)	Membership	Type
				NGC 2204				
TIC 59711686	93.8615525358511	−18.8423139753127	21.08	6693.41 ± 125	3.825	0.5258	F	Misc
				NGC 2262				
TIC 369672843	99.9949396680587	1.1005280367638	14.97	7144.00 ± 140	3.8539	1.0196	F	γ dorodus
				Pismis 18				
TIC 318170024	204.26503754627	−62.1932090248373	7.53	5861.0 ± 330	3.7679	0.8179	F	EW
TIC 318170016	204.208928184582	−62.1923172179637	7.53	3305.0 ± 110	3.5192	2.2570	F	Misc
				NGC 2437				
TIC 94690694	115.823510242526	−14.8329139196625	12.399	7063.26 ± 160	3.8490	1.7134	F	Misc
TIC 94409620	115.510616181402	−14.7741055562133	176.26	9233.0 ± 350	4.0151	2.062	M	Misc
TIC 94322635	115.345435822958	−14.8197453274406	47.04	7870.25 ± 240	3.9514	3.188	M	YSS
TIC 94409484	115.470463684627	−14.7423028495124	16.93	8541.67 ± 170	3.9734	2.169	M	Misc
TIC 94519429	115.647315663641	−15.0468249431276	29.41	9754.67 ± 370	4.0898	2.249	M	SPB
TIC 94322074	115.378758817249	−14.9394523881991	20.63	8745.67 ± 310	3.9466	2.096	M	Misc
TIC 94410959	115.560324659748	15.1116879741543	7.22	8330 ± 180	3.9207	2.623	F	Misc
TIC 94229743	115.278194656648	−14.9725638053055	266.4	4887.25 ± 50	3.8490	1.7134	F	EA

8.1 Classification

8.1.1 γ Dor variable stars

γ Doradus (γ Dor) stars are non-radial gravity-mode (g mode) pulsators with spectral types ranging from A7 to F5. They are found within the γ Dor instability strip on the H–R diagram. This strip designates a transitional zone where stellar energy transport changes from convective cores with radiative envelopes to radiative cores with convective envelopes. As such, γ Dor stars are useful for constraining theoretical models of stellar heat transfer. Their pulsation periods typically range from 0.3 to 3.0 d, with amplitudes of around 0.1 mag. These stars generally have masses between 1.5 and 1.8 M$_\odot$, making them slightly less massive than δ Scuti stars.

One of the variable stars in our sample, TIC 369 672 843 in the open cluster NGC 2262, shows characteristics consistent with a γ Dor classification. It is located within the γ Dor instability strip on the H–R diagram, with a pulsation period of 0.62375 d and an amplitude typical of γ Dor variables. Its effective temperature, 6693.4 K, as reported by Gaia Collaboration (2023), is barely lower than the expected range of 6700–7400 K for γ Dor stars. Based on its pulsation period, amplitude, position on the CMD, and effective temperature, we classify TIC 369 672 843 as a γ Dor variable.

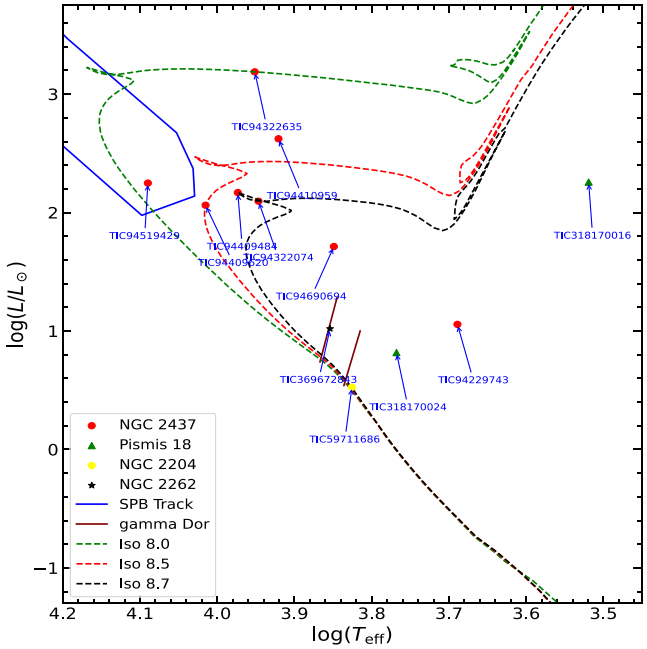

Figure 15. H–R diagram [$\log(T_{\rm eff})$ versus $\log(L/L_{\odot})$] illustrating the positions of candidate and confirmed variable stars in the open clusters NGC 2437, Pismis 18, NGC 2204, and NGC 2262. Coloured symbols denote different clusters. Theoretical instability strips for SPB (solid blue), γ Doradus (brown solid) stars are overplotted, and isochrones of log age 8.0, 8.5, and 8.7 (dashed line).

8.1.2 SPB variable stars

Slowly pulsating B-type (SPB) stars occupy the upper main-sequence region of the H–R diagram and show multiperiodic, non-radial g-mode pulsations driven by the κ mechanism (M. Fedurco et al. 2020). Their typical pulsation periods range from about half a day to several days (A. Stankov & G. Handler 2005). In our study, we identified one bright main-sequence star in NGC 2437, TIC 94519429, with a pulsation period of 1.225416 d, which is well above the 0.42-d threshold, and an effective temperature of 9654.67 K, slightly below 10 000 K. Although the temperature and luminosity values were taken from theoretical isochrones, the star's position on the H–R diagram is consistent with the SPB instability region. Therefore, we classified it as an SPB variable. The corresponding instability strip is marked by the blue line in Fig. 15.

8.1.3 Eclisping binary

Eclipsing binaries play a crucial role in accurately determining stellar masses, luminosities, radii, and distances (K. G. Stassun & G. Torres 2021). In this study, two eclipsing binaries were identified through visual inspection of their light curves. These systems can be recognized photometrically by characteristic features, particularly the depth and shape of the primary and secondary minima, which can be interpreted using Roche lobe geometry. Algol-type (EA) binaries typically involve one component that has filled or overflowed its Roche lobe. Well-defined beginnings and ends of eclipses distinguish their light curves. In contrast, β Lyrae-type (EB) systems, which are semidetached with tidally distorted components, exhibit continuously varying light curves without distinct eclipse boundaries J. Maurya et al. (2023). W Ursae Majoris-type (EW) binaries, also known as W UMa stars, are contact systems with ellipsoidal components and nearly equal depths in their primary and secondary minima. Their light curves lack clearly defined eclipse phases and generally have periods shorter than 1 d.

We found 1 EA reported in C. L. Watson, A. A. Henden & A. Price (2006), E. Avvakumova, O. Y. Malkov & A. Y. Kniazev (2013) and 1 EW reported in C. L. Watson et al. (2006) binaries in the region of NGC 2437 and Pismis 18, respectively. The light curve of eclipsing binaries is shown in the Figs 13 and 14. A detailed analysis of this star is presented in Section 8.2, along with one other eclipsing binary that is part of the field star population.

8.1.4 Yellow stragglers

In the H–R diagram shown in Fig. 15, the star TIC 94 322 635 seems to satisfy the criteria for a YSS as summarized by M. Rain et al. (2021). It is found above the main-sequence turn-off and to the red side of the blue stragglers, which is where YSS usually appear in cluster CMDs. Our identified star is a confirmed member of NGC 2437, with an effective temperature of 7870 K and a pulsation period of 47.04 h. The presence of a YSS in NGC 2437 is significant because this type of star is very rare in open clusters (OCs) and may have formed through complex processes, such as interactions between two stars or mass transfer. Further spectroscopic analysis would help confirm its nature and refine its evolutionary status within the cluster.

Variable stars such as BSS, YSS, and binaries provide important clues to the dynamical evolution of star clusters. Their presence is closely linked to internal cluster processes: BSS and YSS are generally thought to form through mass transfer in binary systems or stellar mergers, both of which are driven by close stellar interactions. In particular, the detection of binaries among BSS underscores the role of binary evolution in shaping the observed stellar populations. Moreover, such interactions also influence the spatial distribution of stars, enhance mass segregation, and accelerate the dynamical evolution of clusters. Consequently, investigating the properties and membership of these variable stars yields valuable insights into stellar interactions, the origin of BSS and YSS, and the overall evolutionary pathways of OCs.

8.1.5 Miscellaneous

A few stars in our sample could not be clearly classified because their positions on the H–R diagram do not match any known regions for variable stars. Seven such stars, TIC 94409620, TIC 94322074, TIC 94409484, TIC 94410959, TIC 59711686, TIC 318170016, and TIC 94690694, fall into this category. Particularly, TIC 94409620, TIC 94322074, and TIC 94409484 lie below the SPB region, which, according to standard models, is normally not associated with pulsating variables. These stars were classified as fast-rotating pulsating B-type (FaRPB) stars in spectroscopic studies by N. Mowlavi et al. (2016), with reported periods shorter than or equal to 0.5 d. However, in our analysis, these stars exhibit periods longer than 0.5 d. Therefore, without any solid evidence, we categorize them as miscellaneous variables in this study.

Future observations should include multiband photometry, long-term monitoring, and targeted spectroscopy to obtain secure classifications of the detected variables. In particular, multiband photometry will help trace colour variations, while long-term monitoring will further refine their periods. Additionally, spectroscopy will provide radial velocities and stellar parameters. The resulting light curves

suggest several possible classifications for the unclassified stars: they may be δ Scuti or γ Doradus pulsators if located near the main sequence, semiregular variables if they are red giants, or eclipsing binaries (e.g. W UMa, Algol systems) if partial eclipses are apparent. The diversity of cluster ages, moreover, implies a wide range of variable-star populations. For example, intermediate-age clusters, such as NGC 2437, are likely to host short-period pulsators and binaries, whereas older clusters, like NGC 2204 and NGC 2660, may contain red giant variables. Notably, despite the richness of NGC 2437, only a few variable stars have been identified in the currently available *TESS* data. To address this gap, continuous CCD monitoring, combined with upcoming *Gaia* variability releases, will be crucial to uncovering additional variables and achieving reliable classifications.

8.2 PHOEBE modelling

Eclipsing binaries show periodic variations in brightness due to their orbital geometry and alignment relative to the observer. Through photometric and spectroscopic techniques, key physical parameters such as orbital period, mass, distance, and stellar radii can be accurately determined. Continuous monitoring of these systems provides valuable insight into their formation and evolutionary processes. In our study, two eclipsing binaries were identified in the open clusters NGC 2437 and Pismis 18. The light curves of these systems were analyzed using the PHOEBE 1.0 (Physics of Eclipsing Binaries; A. Prša & T. Zwitter 2005) modelling software. PHOEBE 1.0, which we used to model eclipsing binaries, is based on the Wilson–Devinney code originally written in FORTRAN. It provides both a graphical user interface (GUI) and a scripting tool, facilitating flexible and detailed analysis.

Two binary stars, TIC 94229743 (NGC 2437) and TIC 318170024 (Pismis 18), are selected as a detached binary and an overcontact binary, respectively, as the fitting models in PHOEBE. The effective temperature estimates available in Gaia Collaboration (2023) are used as the $T_{\rm eff}$ of the primary component for both sources. Stars with effective temperatures ($T_{\rm eff} \leq 7200$ K) are assumed to possess convective envelopes. For these stars, the surface albedo (A), representing the fraction of light reflected, is set to 0.5, whereas the gravity brightening coefficient (g), which accounts for the variation in surface brightness from pole to equator due to rotation, is taken as 0.32. In contrast, stars with radiative envelopes ($T_{\rm eff} \geq 7200$ K) are assigned values of A = 1.0 and g = 1.0. The software automatically updates the limb-darkening coefficients after each iteration, based on the tables provided by W. Van Hamme (1993). Determining the mass ratio ($q = m_2/m_1$) is the first step in modeling the photometric light curve. In the absence of radial velocity data, we employed the q-search method to estimate the mass ratio. Many authors have used this approach (A. Panchal & Y. C. Joshi 2021; F.-X. Li et al. 2023; A. Panchal et al. 2023). In this approach, known parameters such as the time of minimum light, orbital period, and effective temperature ($T_{\rm eff}$) of the primary component are held constant. Meanwhile, other parameters, including the orbital inclination (i), the effective temperature of the secondary component, the surface potential (Ω), and the luminosities of both components (l_1 and l_2) are treated as free parameters during the fitting process. q was varied in small increments, and for each value, a best-fitting model was obtained through multiple iterations. The corresponding cost function was evaluated, and the q value that minimized the cost function was adopted as the optimal mass ratio. This q-search technique was applied to both binary systems, yielding estimated mass ratios of 1.37 for TIC 94229743 and 2.16 for TIC 318170024. Based on these values, we ran the PHOEBE scripter iteratively to refine the final binary star models. The fitted light curves are displayed alongside the observed data in Fig. 16 and the corresponding parameters are shown in Table 7.

In the data set, the light curve of system TIC 94 229 743 exhibits a slight brightness asymmetry. To account for this, one dark spot was

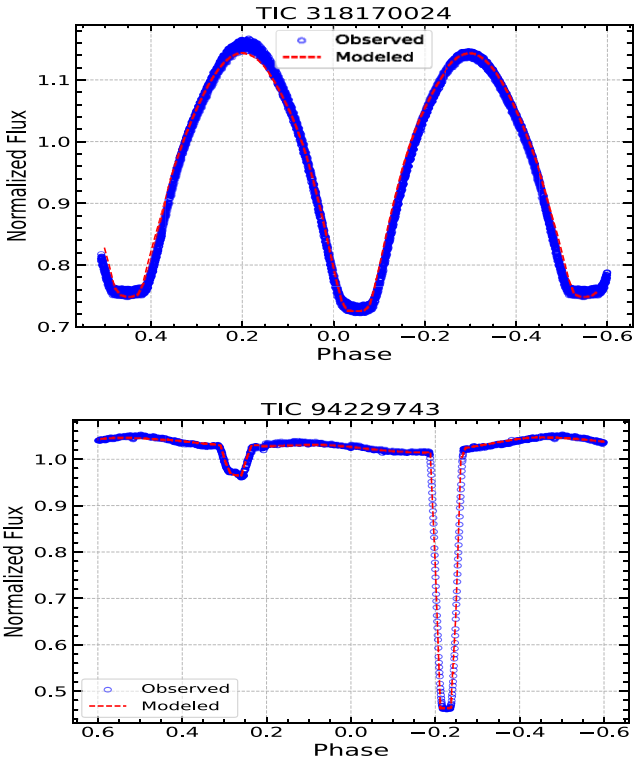

Figure 16. Phase-folded light curves of TIC 318170024 (Pismis 18; top panel) and TIC 94229743 (NGC 2437; bottom panel). Blue points represent the observed *TESS* photometric data, while the red dashed lines indicate the best-fitting models generated using the PHOEBE 1.0 software. These models were used to derive the orbital and physical parameters of the binary systems.

Table 7. Absolute parameters derived from the light curve modelling of TIC 94229743 (NGC 2437) and TIC 318170024 (Pismis 18) using the PHOEBE 1.0 software. The parameters include: orbital period (in days), mass ratio ($q = M_2/M_1$), semimajor axis (a in $R_\odot$), orbital inclination (i in degrees), effective temperatures of the primary ($T_{1\rm eff}$) and secondary ($T_{2\rm eff}$) components in Kelvin, luminosities of the components (l_1, l_2 in $L_\odot$), surface potentials (Ω_1, Ω_2), and radii (R_1, R_2 in $R_\odot$) and masses (M_1, M_2 in $M_\odot$) of the components.

Parameters	**NGC 2437** TIC 94229743	**Pismis 18** TIC 318170024
q	1.37	2.16
i deg	86.6	89.8
$T_{1\rm eff}$ K (fixed)	4887	5861
$T_{2\rm eff}$ K	6670	6100
l_1 ($L_\odot$)	3.958	5.47
l_2 ($L_\odot$)	3.404	4.87
Ω_1	16.30	5.05
Ω_2	7.55	Ω_1
R_1 ($R_\odot$)	1.20	1.446
R_2 ($R_\odot$)	3.12	1.953
M_1 ($M_\odot$)	0.308	0.641
M_2 ($M_\odot$)	0.348	1.385

placed on each stellar component – one on the primary and one on the secondary. The position of a spot on a stellar surface is defined by its colatitude and longitude. The spot colatitude refers to the angular distance from the star's North pole (ranging from 0 to 180°). In contrast, the spot longitude is measured counterclockwise from the direction of the companion star (ranging from 0 to 360°). The spot radius (in degrees) defines the spot's size, and the temperature ratio is the ratio of the spot temperature to the local photospheric temperature. For the spot on the primary component, the adopted parameters are: colatitude = 90° (fixed), longitude = 78° ± 4°, spot radius = 22° ± 2°, and temperature ratio (T_{spot}/T_{star}) = 1.035. For the secondary component, the spot parameters are: colatitude = 90° (fixed), longitude = 164° ± 4°, spot radius = 20° ± 4°, and temperature ratio (T_{spot}/T_{star}) = 0.920.

The evaluated parameters from the PHOEBE light curve modelling should be considered preliminary; improved accuracy will require long-term, multiband photometric observations of these systems. It will also allow for the detection of phenomena such as period changes and stellar surface activity.

9 COMPARATIVE DISCUSSION OF THE SIX CLUSTERS

A comparative assessment of the six clusters (NGC 2204, NGC 2660, NGC 2262, Czernik 32, Pismis 18, and NGC 2437) based on the results in Tables 2, 4, and 5 highlights both shared evolutionary behaviour and cluster-specific differences. We find only a weak tendency for MF slopes to flatten in older systems when considering age. Clusters such as NGC 2204 (∼1.9 Gyr) and NGC 2660 (∼1.5 Gyr) have flatter MF slopes. They also show more centrally concentrated stellar distributions. In contrast, younger clusters like NGC 2437 (∼200 Myr) and Pismis 18 (∼0.7 Gyr) retain larger fractions of low-mass stars in their haloes. This finding broadly supports the idea that dynamical evolution gradually depletes low-mass members and enhances mass segregation. However, the trend remains modest and is not statistically significant across the limited age range of our sample. The mass segregation indices appear nearly constant. This suggests that segregation may be primordial or has reached saturation in these intermediate-age clusters. The comparison of total masses (Table 4) with structural parameters (Table 2) reveals that mass and size are not tightly correlated. The most massive cluster, NGC 2437 (∼2450 $M_\odot$), is also the most extended system, with a large half-mass radius. Clusters of lower mass, such as NGC 2262 (∼268 $M_\odot$) and Czernik 32 (∼350 $M_\odot$), are markedly more compact. This suggests that cluster size is not determined solely by mass. Instead, initial formation conditions and subsequent dynamical processing also influence size. Clusters with similar masses can show substantial differences in compactness. This points to the role of environmental effects, such as tidal shocks or disc crossings. The orbital parameters (Table 5) provide further context. All six clusters are confined to nearly circular, thin-disc orbits (eccentricities 0.02–0.10; $|z| \leq 132$ pc). This configuration helps ensure survival over several hundred Myr. Within this broad similarity, some contrasts are evident. Clusters such as NGC 2204, located at larger Galactocentric distances on circular orbits, retain higher masses and more extended structures. In contrast, NGC 2660, which is closer to the Galactic plane, is more compact. NGC 2262 and Czernik, having similar age and location in the Galaxy, follow similar orbits and have similar sizes. This likely reflects the stronger tidal stresses and repeated disc crossings experienced in its environment. Taken together, these comparisons indicate that mass segregation and MF flattening are universal dynamical signatures. Cluster longevity and present-day structure are determined by an interplay of intrinsic properties (mass, compactness, relaxation time) and extrinsic conditions (orbital parameters, Galactic tides). No single parameter governs cluster evolution across the sample. The results illustrate the complexity of open cluster survival in the Galactic disc. They also point to the importance of expanding such analyses to larger and more diverse cluster sets.

10 CONCLUSIONS

In this work, we carried out a comprehensive investigation of six Galactic open clusters – NGC 2204, NGC 2660, NGC 2262, Czernik 32, Pismis 18, and NGC 2437 – by combining high-precision astrometric data from *Gaia* DR3 with time-series photometry from *TESS*. Our study focused on determining accurate cluster memberships, structural and fundamental parameters, dynamical states, stellar content (including stragglers and variables), and orbital properties. Below, we summarize the key results of our analysis:

(i) We have applied Bayesian and Gaussian Mixture Model (GMM) approaches to determine high-probability cluster members in all studied clusters. The GMM method proved more reliable in minimizing field star contamination, particularly for faint stars with magnitudes between 18 and 20, ensuring a cleaner and more precise selection of cluster membership.

(ii) After fitting King's formula, the structural parameters were calculated for all the clusters, with core radii ranging from 1 to 10 arcmin and overall cluster radii spanning 5 to 24 arcmin. Additionally, the density contrast parameter was estimated to quantify the degree of central concentration. The results show that all the clusters in this study exhibit a relatively high degree of compactness.

(iii) Fundamental parameters, including distance, age, and Galactocentric coordinates, were accurately determined using *Gaia* DR3 data, demonstrating consistency with previous studies and validating the methodologies adopted. The cluster ages, estimated using theoretical isochrones from P. Marigo et al. (2017), range from 0.2 to 2 Gyr, highlighting a diverse set of evolutionary stages. Distances, derived using the Bailer-Jones method, range from 1.76 to 4.20 kpc. All clusters in this study are classified as intermediate-aged and are located within –1.1 to 1.2 kpc from the Galactic plane.

(iv) We identified a total of 13 BSSs and 3 YSSs across multiple OCs, with 7 BSS and 2 YSS in NGC 2204, 2 BSS in NGC 2660, 2 BSS in Czernik 32, 1 BSS in Pismis 18, and 1 BSS along with 1 YSS in NGC 2437. Our findings include previously reported and newly identified BSS, expanding the current catalog of these evolved stellar populations. The observed central concentration of BSS within their respective clusters suggests that their formation is primarily driven by mass transfer in binary systems or stellar collisions. These results offer valuable insights into the dynamic evolution of OCs and stellar interaction processes.

(v) The LFs and MFs were analysed using the most probable cluster members for the six clusters studied. The MF slopes, estimated separately for the core and outer regions, range from 0.96 to 1.19, indicating a shallower distribution than the canonical Salpeter slope (1.35). The observed increase in the MF slope toward the outer regions suggests mass segregation, likely driven by dynamical relaxation processes. This flattening of the MF further implies a higher retention of low-mass stars, providing insights into the dynamical evolution of these clusters.

(vi) Our orbit analysis shows that all six clusters follow low-eccentricity orbits ($e \approx 0.23$–0.10), with perigalactic and apogalactic distances ranging from 5.9 to 12.5 kpc and maximum vertical excursions $|z| \leq 132$ pc. These nearly circular, planar orbits indicate

that the clusters have remained confined to the Galactic thin disc over long time-scales, thereby sustaining their observed dynamical relaxation and resisting disruptive forces. Their confinement in the thin disc is resulting in the quick evaporation of faint stars from the clusters.

(vii) We identified twelve variable stars across four clusters, including one SPB (TIC 94519429), one γ Doradus (TIC 369672843), two eclipsing binaries (TIC 94229743, TIC 318170024), a yellow straggler candidate (TIC 94322635), and several unclassified variables. In the HR diagram, the place and variability properties confirmed their classifications. PHOEBE modelling of the eclipsing binaries demonstrated detached and overcontact configurations, with mass ratios of 1.37 and 2.16, orbital inclinations of 86.6° and 89.8°, and component temperatures in the range of 6100–6760 K. These binaries offer robust constraints on stellar parameters and binary evolution in cluster environments.

ACKNOWLEDGEMENTS

We thank the referee for the constructive comments and suggestions that have helped to improve this manuscript. We are also grateful to the editor for valuable comments regarding the presentation of figures. Ing-Guey Jiang acknowledges the support from the National Science and Technology Council (NSTC), Taiwan, with a grant NSTC 113-2112-M-007-030. This work has utilized data from the European Space Agency (ESA) mission *Gaia* (https://www.cosmos.esa.int/gaia), processed by the *Gaia* Data Processing and Analysis Consortium (DPAC, https://www.cosmos.esa.int/web/gaia/dpac/consortium). The DPAC is funded by national institutions, particularly those participating in the *Gaia* Multilateral Agreement. The Digitized Sky Surveys were produced at the Space Telescope Science Institute under U.S. Government grant NAG W-2166. This study also utilizes data obtained by the *Transiting Exoplanet Survey Satellite* (*TESS*) mission, funded by NASA's Explorer Program.

PYTHON modules: NUMPY (1.19.0; C. R. Harris et al. 2020), SCIPY (v1.3.1; E. Jones et al. 2001), and MATPLOTLIB (v3.1.1; J. D. Hunter 2007).

DATA AVAILABILITY

This work is based on two publicly available data sets: *Gaia* DR3 and *TESS*, for the clusters NGC 2204, NGC 2660, NGC 2262, Czernik 32, Pismis 18, and NGC 2437. The *Gaia* DR3 data can be accessed at: https://gea.esac.esa.int/archive/. The *TESS* data used in this study are publicly available through the Mikulski Archive for Space Telescopes (MAST): https://mast.stsci.edu/.

REFERENCES

Agarwal M., Rao K. K., Vaidya K., Bhattacharya S., 2021, MNRAS, 502, 2582
Angelo M., Santos Jr J., Corradi W., 2020, MNRAS, 493, 3473
Angelo M., Santos Jr J., Maia F., Corradi W., 2023, MNRAS, 522, 956
Anthony-Twarog B. J., Deliyannis C. P., Steinhauer A., Sun Q., Twarog B. A., 2024, AJ, 168, 103
Asplund M., Grevesse N., Sauval A. J., Scott P., 2009, ARA&A, 47, 481
Avvakumova E., Malkov O. Y., Kniazev A. Y., 2013, Astron. Nachr., 334, 860
Bailer-Jones C., Rybizki J., Fouesneau M., Mantelet G., Andrae R., 2018, AJ, 156, 58
Balaguer-Núnez L., Tian K., Zhao J., 1998, A&AS, 133, 387
Belwal K., Bisht D., Bisht M. S., Rangwal G., Raj A., Dattatrey A. K., Yadav R., Bhatt B., 2024, AJ, 167, 188
Bica E., Bonatto C., 2005, A&A, 443, 465
Bisht D., Yadav R., Ganesh S., Durgapal A., Rangwal G., Fynbo J., 2019, MNRAS, 482, 1471
Bisht D., Zhu Q., Yadav R., Durgapal A., Rangwal G., 2020, MNRAS, 494, 607
Bisht D., Zhu Q., Elsanhoury W. H., Sariya D. P., Rangwal G., Yadav R. S., Durgapal A., Jiang I.-G., 2021a, PASJ, 73, 677
Bisht D., Zhu Q., Yadav R., Rangwal G., Durgapal A., Sariya D. P., Jiang I.-G., 2021b, AJ, 161, 182
Bisht D., Zhu Q., Yadav R., Rangwal G., Sariya D. P., Durgapal A., Jiang I.-G., 2022a, PASP, 134, 044201
Bisht D., Zhu Q., Elsanhoury W., Yadav R., Rangwal G., Sariya D. P., Durgapal A., Jiang I.-G., 2022b, AJ, 164, 171
Bisht D., Bisht D., Raj A., Rangwal G., Sariya D. P., Manu M., 2024, New Astron., 109, 102205
Bonatto C., Bica E., 2007, MNRAS, 377, 1301
Bonatto C., Bica E., Santos Jr J. F., 2008, MNRAS, 386, 324
Bovy J., 2015, ApJS, 216, 29
Bragaglia A. et al., 2024, A&A, 687, A124
Cantat-Gaudin T. et al., 2020, A&A, 640, A1
Carraro G., Baume G., Vázquez R., Moitinho A., Geisler D., 2005, MNRAS, 362, 649
Casagrande L., VandenBerg D. A., 2018, MNRAS, 479, L102
Castro-Ginard A., Jordi C., Luri X., Cantat-Gaudin T., Balaguer-Núñez L., 2019, A&A, 627, A35
Chen X., Wang S., Deng L., De Grijs R., Yang M., Tian H., 2020, ApJS, 249, 18
Cover T., Hart P., 1967, IEEE Trans. Inf. Theory, 13, 21
Dattatrey A. K., Yadav R., Rani S., Subramaniam A., Singh G., Sahu S., Singh R. S., 2023, ApJ, 943, 130
Davidge T., 2013, PASP, 125, 115
de Graeve E., 1979, Vatican Observatory Publications, 1, 283
Dempster A. P., Laird N. M., Rubin D. B., 1977, J. R. Stat. Soc: Series B (Methodological), 39, 1
Dias W. S., Monteiro H., Moitinho A., Lépine J. R., Carraro G., Paunzen E., Alessi B., Villela L., 2021, MNRAS, 504, 356
Dib S., Kim J., Shadmehri M., 2007, MNRAS, 381, L40
Fedurco M., Paunzen E., Hümmerich S., Bernhard K., Parimucha Š., 2020, A&A, 633, A122
Ferraro F. R. et al., 2009, Nature, 462, 1028
Freeman K., Bland-Hawthorn J., 2002, ARA&A, 40, 487
Friel E., 1995, ARA&A, 33, 381
Gaia Collaboration, 2023, A&A, 674, A41
Gao X., 2018, ApJ, 869, 9
Gautschy A., Saio H., 1993, MNRAS, 262, 213
Geller A. M., Mathieu R. D., Braden E. K., Meibom S., Platais I., Dolan C. J., 2010, AJ, 139, 1383
Gieles M., Zwart S. P., Baumgardt H., Athanassoula E., Lamers H., Sipior M., Leenaarts J., 2006, MNRAS, 371, 793
Girard T. M., Grundy W. M., López C. E., van Altena W. F., 1989, AJ, 98, 227
Groenewegen M., 2021, A&A, 654, A20
Gustafsson B., Church R. P., Davies M. B., Rickman H., 2016, A&A, 593, A85
Harris C. R. et al., 2020, Nature, 585, 357
Hatzidimitriou D. et al., 2019, A&A, 626, A90
Hills J., Day C., 1976, ApJ, 17, 87
Hoq S., Clemens D., 2015, AJ, 150, 135
Hunt E. L., Reffert S., 2023, A&A, 673, A114
Hunter J. D., 2007, Comput. Sci. Eng., 9, 90
Iorio G., Belokurov V., 2019, MNRAS, 482, 3868
Jadhav V. V., Roy K., Joshi N., Subramaniam A., 2021, AJ, 162, 264
Jeffery E. J., von Hippel T., van Dyk D. A., Stenning D. C., Robinson E., Stein N., Jefferys W. H., 2016, ApJ, 828, 79
Jiang D., Han Z., Li L., 2014, MNRAS, 438, 859
Jones E., Oliphant T., Peterson P. et al., 2001, SciPy: Open Source Scientific Tools for Python.
Kang Y. B., Kim S.-L., Rey S.-C., Lee C.-U., Kim Y., Koo J.-R., Jeon Y.-B., 2007, PASP, 119, 239

Kharchenko N., Piskunov A., Schilbach E., Röser S., Scholz R.-D., 2013, A&A, 558, A53
King I., 1962, AJ, 67, 471
Kroupa P., Boily C. M., 2002, MNRAS, 336, 1188
Li F.-X. et al., 2023, ApJ, 956, 49
Lindegren L. et al., 2021, A&A, 649, A2
Lloyd S., 1982, IEEE Trans. Inf. Theory, 28, 129
Lomb N. R., 1976, Astrophys. Space Sci., 39, 447
MacQueen J. et al., 1967, in Proc. 5th Berkeley Symposium on Mathematical Statistics and Probability. Univ. California Press, California, p. 281
Magrini L. et al., 2023, A&A, 669, A119
Mapelli M., Sigurdsson S., Ferraro F. R., Colpi M., Possenti A., Lanzoni B., 2006, MNRAS, 373, 361
Marigo P. et al., 2017, ApJ, 835, 77
Maurya J., Joshi Y. C., Panchal A., Gour A., 2023, AJ, 165, 90
McCrea W., 1964, MNRAS, 128, 147
McLachlan G., Peel D., 2000, Finite Mixture Models. Wiley-Interscience, New York, p. 419
Mowlavi N., Saesen S., Semaan T., Eggenberger P., Barblan F., Eyer L., Ekström S., Georgy C., 2016, A&A, 595, L1
Naoz S., Fabrycky D. C., 2014, ApJ, 793, 137
Netopil M., Paunzen E., Heiter U., Soubiran C., 2016, A&A, 585, A150
Panchal A., Joshi Y. C., 2021, AJ, 161, 221
Panchal A., Joshi Y., De Cat P., Lampens P., Goswami A., Tiwari S., 2023, MNRAS, 521, 677
Panwar N., Rishi C., Sharma S., Ojha D. K., Samal M. R., Singh H., Yadav R. K., 2024, AJ, 168, 89
Phelps R. L., Janes K. A., 1993, AJ, 106, 1870
Piatti A. E., Clariá J. J., Bica E., Geisler D., Minniti D., 1998, AJ, 116, 801
Portegies Zwart S. F., McMillan S. L., Gieles M., 2010, ARA&A, 48, 431
Prša A., Zwitter T., 2005, ApJ, 628, 426
Qiu J.-S., Zhu Q.-F., Li X.-Z., Xu X.-H., Zheng H., 2024, ApJ, 967, 94
Rain M., Ahumada J., Carraro G., 2021, A&A, 650, A67
Rangwal G., Yadav R., Bisht D., Durgapal A., Sariya D. P., 2023, MNRAS, 523, 1867
Rangwal G., Arya A., Subramaniam A., Singh K. P., Liu X., 2025, J. Astrophys. Astron., 46, 52
Ricker G. R. et al., 2015, J. Astron. Telesc. Instrum. Syst., 1, 014003
Šablevičiūtė I., Vansevičius V., Kodaira K., Narbutis D., Stonkutė R., Bridžius A., 2006, Baltic Astron., 15, 547
Sagar R., Griffiths W., 1998, MNRAS, 299, 777
Salpeter E. E., 1955, ApJ, 121, 161
Sánchez N., Alfaro E. J., López-Martínez F., 2020, MNRAS, 495, 2882
Sandage A., 1953, AJ, 58, 61
Sandrelli S., Bragaglia A., Tosi M., Marconi G., 1999, MNRAS, 309, 739
Sariya D. P. et al., 2021, AJ, 161, 101
Scargle J. D., 1982, ApJ, 263, 835
Sharma S., Pandey A., Ogura K., Mito H., Tarusawa K., Sagar R., 2006, AJ, 132, 1669
Sheikh A., Deka S., Medhi B. J., 2025, MNRAS, 536, 174
Skowron D. M. et al., 2019, Science, 365, 478
Soubiran C. et al., 2018, A&A, 619, A155
Spitzer Jr L., Hart M. H., 1971, ApJ, 166, 483
Stankov A., Handler G., 2005, ApJS, 158, 193
Stassun K. G., Torres G., 2021, ApJ, 907, L33
Tadross A. L., 2008, New Astron., 13, 370
Torres G., Andersen J., Giménez A., 2010, A&AR, 18, 67
Twarog B. A., Ashman K. M., Anthony-Twarog B. J., 1997, AJ, 114, 2556
Valle G., Dell'Omodarme M., Tognelli E., 2021, A&A, 649, A127
Van Hamme W., 1993, AJ, 106, 2096
Watson C. L., Henden A. A., Price A., 2006, in 25th Annual Symposium on Telescope Science. Society for Astronomical Sciences, California, p. 47
Wielen R., 1971, A&A, 13, 309
Yadav R., Sariya D. P., Sagar R., 2013, MNRAS, 430, 3350
Yadav R., Dattatrey A. K., Rangwal G., Subramaniam A., Bisht D., Sagar R., 2024, ApJ, 961, 251
Zhong J., Chen L., Wu D., Li L., Bai L., Hou J., 2020, A&A, 640, A127

APPENDIX A: MEMBERSHIP PLOT

We conducted a comprehensive photometric and kinematic study of six intermediate-age open clusters (OCs): NGC 2204, NGC 2660, NGC 2262, Czernik 32, Pismis 18, and NGC 2437, utilizing data from *Gaia* DR3. Membership probabilities were evaluated within the regions of these clusters, identifying the most probable members, defined as those with membership probabilities exceeding 70 per cent. The corresponding plots for the remaining clusters are presented in Fig. A1 in the Appendix.

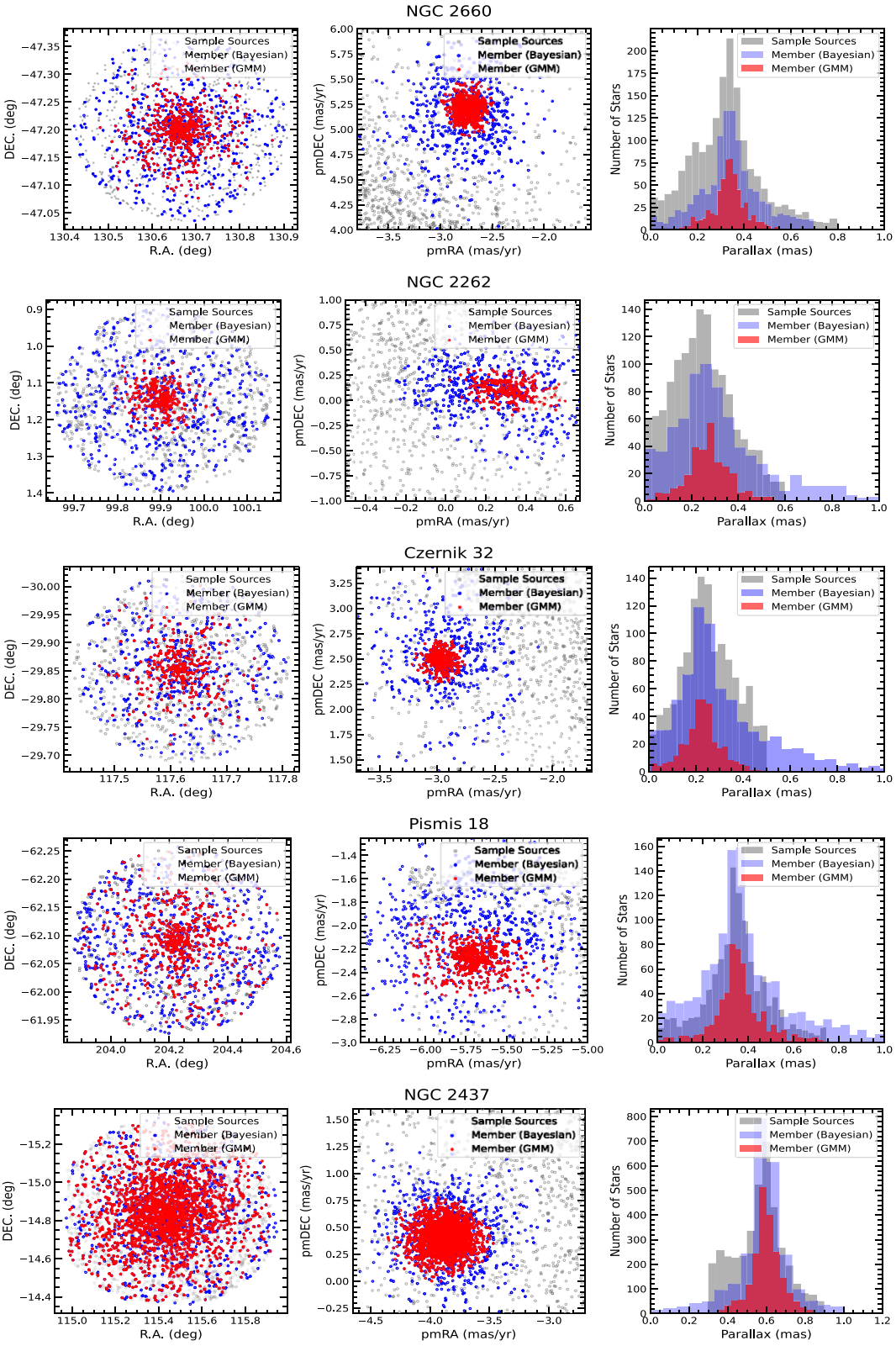

Figure A1. (a) The spatial distribution, (b) proper motion distribution, and (c) parallax distribution using ML-MOC algorithm and Bayesian approach on *Gaia* DR3 data.

APPENDIX B: COMPARISON PLOT

The corresponding plots for the remaining clusters are presented in Fig. B1 in the Appendix.

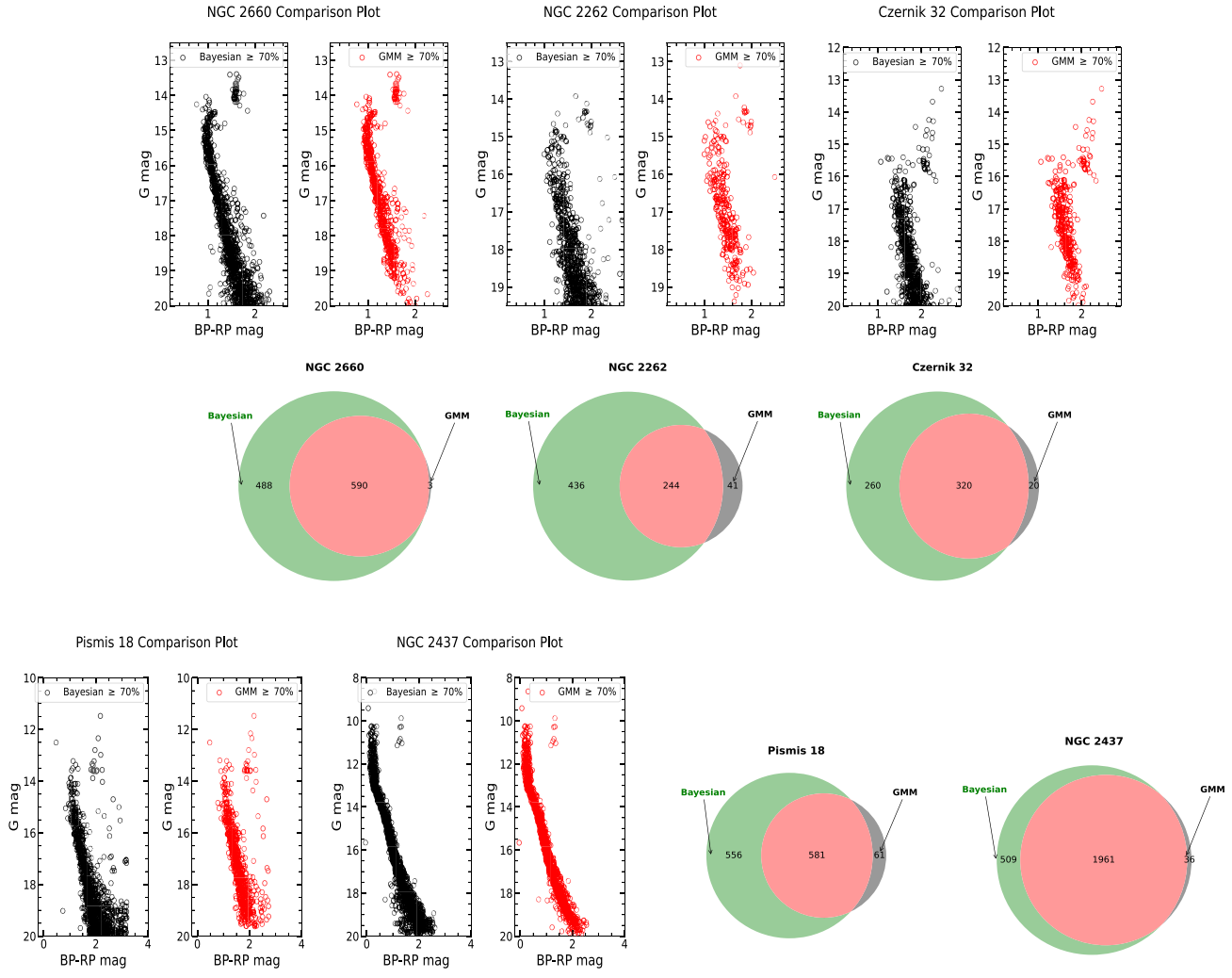

Figure B1. Comparison plot and Venn diagram for the Bayesian approach and Gaussian Mixture Model using cluster members with a probability of ≥70 per cent.

This paper has been typeset from a TEX/LATEX file prepared by the author.